

Towards A Mobile Damping Robot For Vibration Reduction of Power Lines

Paul-Camille Kakou

Thesis submitted to the Faculty of the
Virginia Polytechnic Institute and State University
in partial fulfillment of the requirements for the degree of

Master of Science
in
Mechanical Engineering

Oumar Barry, Chair
Corina Sandu
Lei Zuo

April 27, 2021
Blacksburg, Virginia

Keywords: Wind-induced vibration control, energy harvesting, mobile damping robot

Copyright 2021, Paul-Camille Kakou

Towards A Mobile Damping Robot For Vibration Reduction of Power Lines

Paul-Camille Kakou

(ABSTRACT)

As power demand across communities increases, focus has been given to the maintenance of power lines against harsh environments such as wind-induced vibration (WIV). Currently, inspection robots are used for maintenance efforts while fixed tuned mass dampers (FTMDs) are used to prevent structural damages. However, both solutions are facing many challenges. Inspection robots are limited by their size and considerable power demand, while FTMDs are narrowband and unable to adapt to changing wind characteristics, and thus are unable to reposition themselves at the antinodes of the vibrating loop. In view of these shortcomings, we propose a mobile damping robot (MDR) that integrates inspection robots' mobility and FTMDs WIV vibration control to help maintain power lines. In this effort, we model the conductor and the MDR by using Hamilton's principle and we consider the two-way nonlinear interaction between the MDR and the cable. The MDR is driven by a Proportional-Derivative controller to the optimal vibration location (i.e, antinodes) as the wind characteristics vary. The numerical simulations suggest that the MDR outperforms FTMDs for vibration mitigation. Furthermore, the key parameters that influence the performance of the MDR are identified through a parametric study. The findings could set up a platform to design a prototype and experimentally evaluate the performance of the MDR.

Towards A Mobile Damping Robot For Vibration Reduction of Power Lines

Paul-Camille Kakou

(GENERAL AUDIENCE ABSTRACT)

Power lines are civil structures that span more than 160000 miles across the United States. They help electrify businesses, factories and homes. However, power lines are subject to harsh environments with strong winds, which can cause Aeolian vibration. Vibration in this context corresponds to the oscillation of power lines in response to the wind. Aeolian vibration can cause significant structural damages that impact public safety and result in a significant economic loss. Today, different solutions have been explored to limit the damages to these key structures. For example, the lines are commonly inspected by foot patrol, helicopters, or inspection robots. These inspection techniques are labor intensive and expensive. Furthermore, Stockbridge dampers, mechanical vibration devices, can be used to reduce the vibration of the power line. However, Stockbridge dampers can get stuck at location called nodes, where they have zero efficiency. To tackle this issue, we propose a mobile damping robot that can re-adjust itself to points of maximum vibration to maximize vibration reduction. In this thesis, we explore the potential of this proposed solution and draw some conclusions of the numerical simulations.

Dedication

To my parents Sylvain and Evelyne, and my siblings Anne-Philippe and Louis-David.

Acknowledgments

First of all, I would like to thank GOD for the blessings and gifts He has bestowed upon me. I am deeply grateful to my advisor and mentor Dr. Oumar Barry for his guidance, his unwavering support, constant encouragement, and insight throughout my work. He influenced me in pursuing research in vibrations and controls, and provided the platform necessary for my success. I would also like to extend my sincere thanks to my committee members Dr. Corina Sandu and Dr. Lei Zuo for their valuable suggestions to my thesis. I am also grateful for my labmates whom have participated in this positive learning experience as well as my girlfriend Angel Isiadinso for her continued support. Finally, I would like to thank the partial financial support from Virginia Tech and the NSF Grant.

Contents

- List of Figures viii

- List of Tables xii

- 1 Background and Literature Review 1**
 - 1.1 Problem presentation 1
 - 1.2 Current solutions 2
 - 1.2.1 Vibration mitigation 2
 - 1.2.2 Structural health monitoring 7
 - 1.3 Proposed solution 9
 - 1.3.1 Mechanical design and considerations 11
 - 1.3.2 Energy harvesting of WIV 12
 - 1.3.3 Modeling considerations 13
 - 1.4 Objectives and Contributions of the Thesis 14
 - 1.5 Thesis Organization 15

- 2 Vibration Suppression Control: Power lines 17**
 - 2.1 System Description and Modeling 17
 - 2.1.1 Modeling the MDR 18

2.1.2	Modeling the MDR with the energy harvester	25
2.2	Validation using the Harmonic Balance method	26
3	Results	29
3.1	Validation and numerical considerations	29
3.2	Mobile damping robot performance	31
3.2.1	Proportional and derivative gain for optimal control	31
3.2.2	Comparing the fixed absorber to the MDR	33
3.2.3	Optimal mass ratio for vibration control	43
3.2.4	Two mobile damping robots	45
3.2.5	Energy requirement of the mobile damping robot	47
3.3	Energy harvesting mobile damper performance	47
3.3.1	Comparing the EHMDR to the MDR	48
4	Discussion	54
5	Conclusions and Future work	56
5.1	Conclusions	56
5.2	Future Work	57
	Bibliography	59
	Appendix A Matlab code	72

List of Figures

- 1.1 Power line failure due to WIV in Ontario 2
- 1.2 Original (a) and modern (b) symmetric Stockbridge damper design. 4
- 1.3 Asymmetric Stockbridge damper design with 4 resonant frequencies. 5
- 1.4 Asymmetric Stockbridge damper design with six and more resonant frequencies. 5
- 1.5 Six resonant modes of the recent patented Asymmetric Stockbridge damper
[15, 81]. 6
- 1.6 Ineffectiveness of a Stockbridge damper resulting in failure of a power line
with broken strands. 7
- 1.7 Manned repair of a power line. 8
- 1.8 A helicopter-assisted repair of a power line 8
- 1.9 Hydro Quebec Linescout inspection robot 10
- 1.10 The transmission line inspection robot developed by EPRI. 10
- 1.11 Conceptual design of the MDR attached to a power line cable. 11
- 2.1 Schematic of the MDR on the cable 17
- 2.2 PD controller feedback loop that helps track the target antinode r 21
- 3.1 A comparison between analytical and numerical simulation for the fixed damper. 30

3.2	Determining the number of modes required for the numerical simulation. Figure 3.2-(a) considers the vibration of the bare beam while (b) consider the vibration of the beam with a fixed damper.	31
3.3	Determining the values of k_p and k_d for optimal control	32
3.4	Determining the values of k_p and k_d for optimal control	34
3.5	Frequency response of the cable and the robot along the span. Figure 3.5-(a) shows the transmissibility of the cable as a function of the normalized frequency. Figure 3.5-(b) shows the transmissibility of the cable with a damper attached as a function of the normalized frequency.	35
3.6	Time functions and time response of the cable comparing the performance of the fixed damper against the MDR for $\omega_e = \omega_1$	36
3.7	A comparison of the vibration control performance of the fixed damper and the proposed MDR for (a) ω_3 , (b) ω_9 , (c) ω_{13} and (d) ω_{17}	38
3.8	Final location of the fixed damper and the mobile damper for varying input excitation.	39
3.9	Comparing the normalized work done on the cable for the fixed damper and the MDR for varying normalized frequency.	40
3.10	Comparing the efficiency of the fixed damper to the MDR for varying normalized frequencies.	41
3.11	Time response for different damping conditions when the initial location of the dampers coincide with a node.	42

3.12	Performance of the dampers when the initial location coincide with a node. Figure 3.12-(a) shows the normalized power across the cable length for each damping conditions for the nodal case. Figure 3.12-(b) shows normalized power across the cable length for each damping conditions when the fixed damper is at its optimal location for reference. Figure 3.12-(c) shows the efficiency of each damper when the both dampers are initially placed at different locations across a vibrating loop.	43
3.13	Comparing the steady state normalized displacement of the cable for each damping condition for varying normalized frequencies.	44
3.14	Effect of varying the relative mass ratio of the MDR. The analysis considers (a) the normalized power output, (b) the normalized work done on the cable, and (c)the dampers efficiency.	45
3.15	Comparing the normalized power on the cable for the fixed damper, a single MDR and two MDR as a function of normalized length.	46
3.16	Assessing the energy requirement of the MDR as a function of the normalized input frequency.	48
3.17	A comparison of the vibration control performance of the fixed damper, the MDR and the EHMDR for (a) ω_3 , (b) ω_9 , (c) ω_{13} and (d) ω_{17}	49
3.18	Time functions and time response of the cable comparing the performance of the EHMDR to the other dampers for ω_1 (Fig. 3.18 (a)-(c)).	50
3.19	Assessing (a) the amount of work done on the cable and (b) the efficiency for the EHMDR when compared to the EHMDR.	51

3.20 Comparing the energy output of the controller to the energy harvested by the EHMDR.	52
3.21 Determining the power harvested by the EHMDR when the cable is excited by the first and the third mode.	53

List of Tables

3.1	Parameters of the conductor and the applied load	30
3.2	Parameters of the EHMDR	49

List of Abbreviations

\dot{q}	Current variation in the RLC circuit (A)
η	Efficiency of the mobile damping robot
ω_e	Wind excitation frequency (rad/s)
ω_n	Natural frequency (rad/s)
Φ	Normalized displacement function
A	The assumed normalized time functions
C	Capacitance of the electromagnetic transducer (H)
c	Damper constant (N s/m)
E_k	The total kinetic energy (J)
E_{disp}	The energy dissipated by the mobile robot damping device
E_{harv}	The energy harvested by the mobile robot damping device
E_{kb}	Kinetic energy of the beam (J)
E_{kd}	Kinetic energy of the suspended absorber (J)
E_{kr}	Kinetic energy of the robot (J)
EI	Flexural rigidity of the conductor (Nm^2)
$F(x, t)$	The applied axial wind force (N)

f_0	The amplitude of the wind force (N)
F_1	Force due to the in-span mobile device (N)
F_2	Force due to the absorber (N)
k	Spring constant (N/m)
k_f	Electromagnetic transducer force constant
k_v	Electromagnetic transducer voltage constant
L	The length of the beam (m)
L_i	Inductance of the electromagnetic transducer (H)
m	Mass per unit length of the beam (kg/m)
m_d	Mass of the suspended absorber (kg)
m_r	Mass of the in-span robot (kg)
R	Resistance of the electromagnetic transducer (Ω)
T	Cable tension (N)
t	Time (s)
W	Work done by the wind force on the conductor (J)
x_r	Position of the mobile damping robot (m)
y	The transverse displacement of the conductor (m)
y_d	Transverse displacement of the absorber at location (m)

Chapter 1

Background and Literature Review

1.1 Problem presentation

Buildings, bridges, overhead transmission lines and other continuum systems are essential as human strive for high-quality lives. For example, the supply of electricity has become a basic necessity in modern society. However, civil structures such as power lines are subject to undesirable vibrations that lead to damages. Wind-induced vibration (WIV) [40] is an example of undesirable vibration for engineering structures, such as suspended roofs, guyed lattice towers, wind turbines, spacecraft, power lines, and cable-stayed bridges. This thesis focuses on Aeolian vibration of single overhead conductor. Aeolian vibration is a type of WIV characterized by a small-amplitude and high frequency motion. The motion arises from alternating forces caused by vortex shedding. The result of this movement is a bending stress at restraints causing abrasion and fatigue over time. Power lines are also subject to two other types of WIV which are galloping and wake-induced oscillation. Galloping has a low frequency (1-3 Hz) and large amplitude motion [7, 26, 53]. Wake-induced oscillation is restricted to bundle conductors and is characterized by medium amplitude of vibration and higher natural frequencies [4, 50].

Aeolian vibration frequencies generally vary between 3 Hz and 150 Hz, and the peak-to-peak amplitude can be the same as the cable diameter [8, 11, 12, 16, 22, 52, 82, 83]. Left uncontrolled, WIV can lead to power lines failure, thereby undermining public safety and



Figure 1.1: Power line failure due to WIV in Ontario

resulting in considerable economic loss. The Department of Energy (DOE) reported that weather-related annual outage costs were estimated to be between \$18 and \$33 billion [64]. While WIV is only responsible for a small percentage of this, the costs are still enormous. In March 2017, DTE Energy Co. reported that a WIV caused power outage to more than 4,000 customers [65]. Similar power outages due to WIV were reported in Ontario leaving millions of customers without power (Fig. 1.1).

1.2 Current solutions

1.2.1 Vibration mitigation

The conventional methodology for vibration mitigation employs tuned mass dampers (TMD). The first TMD was designed by Frahm *et. al*, [33]. TMD consist of a secondary mass, a spring, and a viscous damper; it is attached to a primary or main vibratory system to reduce

its dynamic motion. Since the initial development of TMD, several researchers have optimized linear vibration control solutions based on tuned dampers via passive [47, 56, 61, 78], semi-active [41, 46, 70] and active [37, 49, 80] means. Passive TMD are favored for their structural simplicity and good stability, but they are significantly limited in applications where the primary structure encounters broadband disturbances. Moreover, the deterioration of passive TMD structural parameters over time decreases their efficiency. To overcome passive TMD limitations, active TMD have been implemented. Active dampers consist of sensors and actuators coupled with a controller that drives the absorber to suppress the vibration of the system. However, the performance of active dampers suffers from control-induced instability. Recently, emphasis has been given to semi-active dampers, which combine the benefits of passive and active TMD by using a control scheme that tunes the passive device parameters such as the stiffness of the absorber.

For power lines, the Stockbridge damper (SD), which is a passive tuned mass damper, is commonly used for Aeolian vibration reduction. The Stockbridge damper was first developed by George H. Stockbridge in 1925 [76] (Fig. 1.2). This first development of the damping device is termed as symmetric Stockbridge damper or 2R damper since the counterweights on both sides are symmetric, and the system possesses two resonant frequencies in the Aeolian vibration frequency range. Figure 1.2-(a) shows that the original design used concrete blocks as counterweights. With modern technology, Fig. 1.2-(b) shows an updated design with steel counterweights. With the help of SD, the vibration of the conductor is transferred and reduced by the damper masses. The effectiveness of Stockbridge dampers depends on two main aspects [8, 12, 14, 16, 27, 52, 81]. First, the effectiveness of SD is a function of the number of resonant frequency they exhibit (i.e., dampers natural frequency matching excitation frequency). To extend the number of resonant frequencies of SD, the modern designs have been modified to have one of the rigid mass greater than the other and also

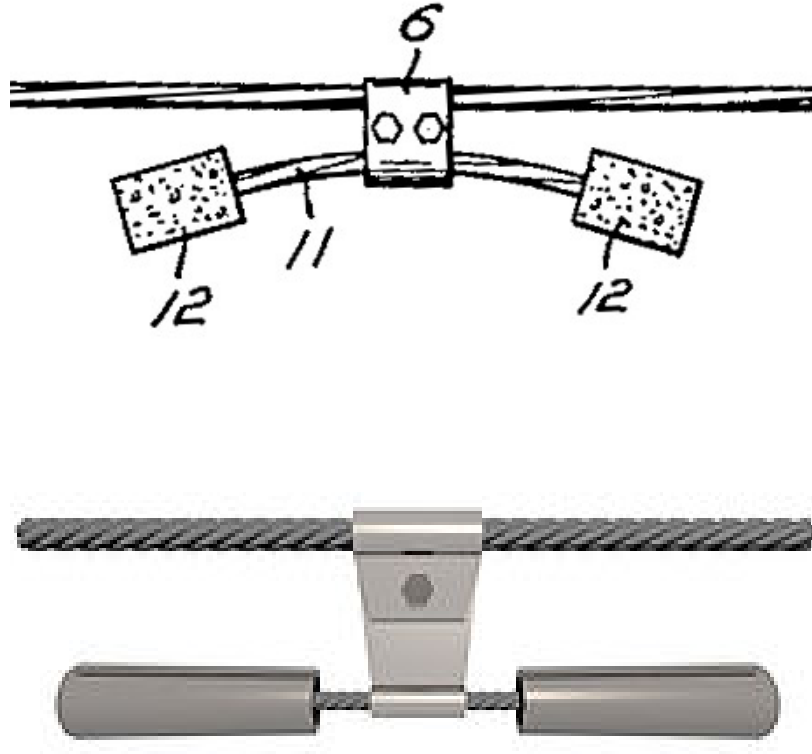


Figure 1.2: Original (a) and modern (b) symmetric Stockbridge damper design.

unequal length on either side of the messenger cable. In this case, the Stockbridge damper is termed Asymmetric Stockbridge damper and it possesses four resonant frequencies [13] (Fig. 1.3). The significance of this is that the damper action is maximum at its resonant frequencies and is less effective as we move away from the resonant frequencies. Having four resonant frequencies as opposed to two give us a greater damping over the entire spectrum of Aeolian vibration frequencies and also increase the fatigue life of damper itself [55].

The ability to increase the efficiency of the damping robot in terms resonant frequencies has been a center of research for the last two decades. Recently, Barry *et. al.*, [15, 81] patented a new asymmetric damper cable to cover between six to ten resonant frequencies (See Fig. 1.4). This updated design relies on changing the geometry of the counterweight by having



Figure 1.3: Asymmetric Stockbridge damper design with 4 resonant frequencies.

one side of a single counterweight larger than the other. Figure 1.5 shows the six resonant modes of the Asymmetric Stockbridge damper obtained using Solidworks. This adaptation of the Stockbridge can be resized to fit a selected conductor.

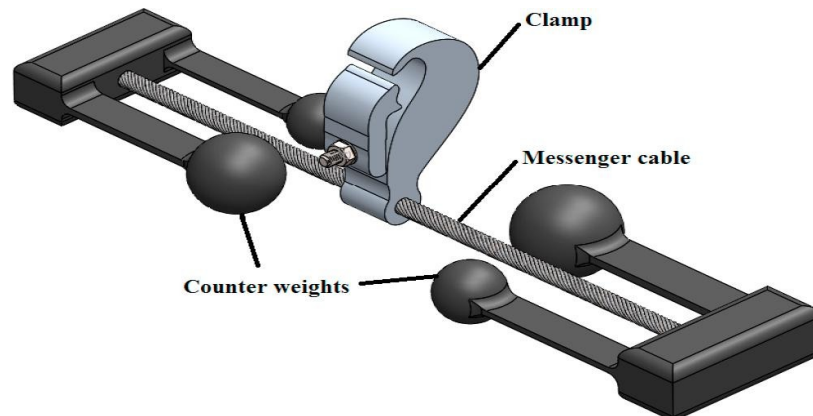


Figure 1.4: Asymmetric Stockbridge damper design with six and more resonant frequencies.

The effectiveness of the SD also depends on its location on the conductor. The ideal location of SD is the antinode (point of maximum amplitude) of the vibrating loop. However, because vibrating loop length depends on wind velocity, the assurance of the relative position of a fixed damper with respect to an antinode is practically impossible. There are numerous studies that focused on the optimum placement of Stockbridge dampers closer to antinodes [9, 10, 52, 69], but none guarantee reasonable performance at every wind frequency. This is primarily because the change in frequency with varying wind speed can cause the location of

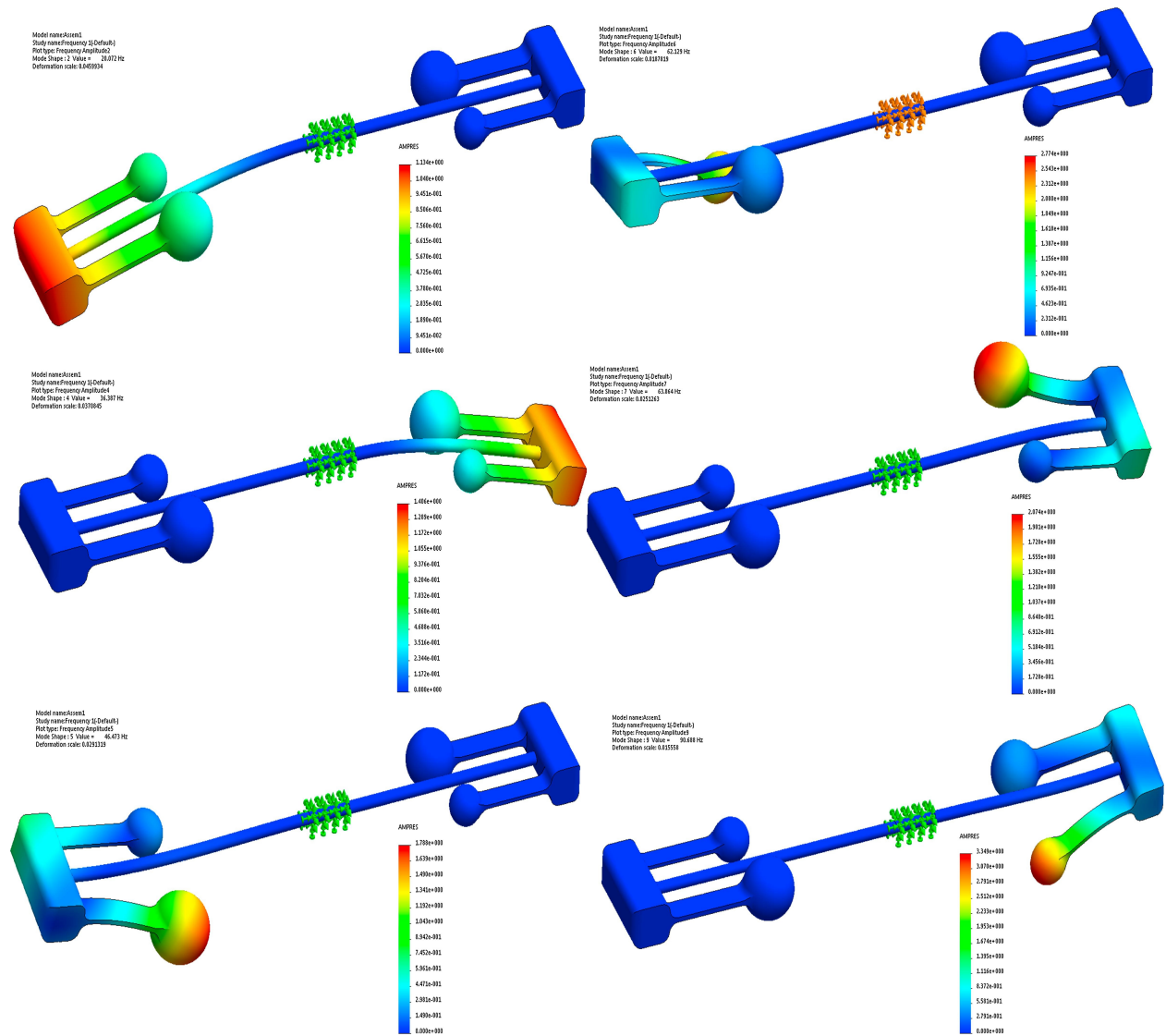


Figure 1.5: Six resonant modes of the recent patented Asymmetric Stockbridge damper [15, 81].

the damper to coincide with a node, thus resulting in poor performance. For example, Fig. 1.6 shows a power line with broken strands. In the Fig. we can also observe the presence of a Stockbridge damper. The failure of the line with a damper shows the limitations of the Stockbridge damper.

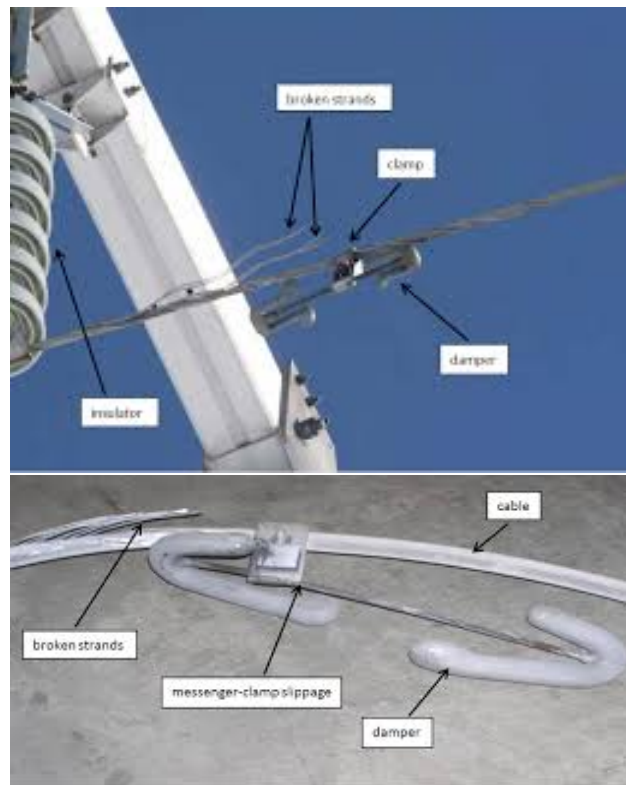


Figure 1.6: Ineffectiveness of a Stockbridge damper resulting in failure of a power line with broken strands.

1.2.2 Structural health monitoring

Beyond vibration mitigation, there exist methods for power line structural health monitoring such as foot patrol (See Fig. 1.7), and helicopter-assisted inspection [5, 42, 43] (See Fig. 1.8). Foot-patrol is carried out by two or more individuals. The inspection can be done visually using infrared and corona detection cameras. Visual inspections are only accurate

to detect surface defects. Because the lines are long and sometimes isolated in harsh environments, visual inspection is slow, tedious, dangerous and sometimes impossible. To expedite visual inspection of the power lines, helicopter-assisted inspection has been considered. For helicopter-assisted inspection, a pilot flies the aircraft while the camera operator films the conductor. Helicopter-assisted inspection is faster than foot-patrol. However, due to the vibrations and movement of the helicopter, it is difficult to obtain high-quality images of the line and locate possible defects. Helicopter-assisted inspection is also an expensive solution considering fuel cost.



Figure 1.7: Manned repair of a power line.



Figure 1.8: A helicopter-assisted repair of a power line

To resolve the aforementioned shortcomings of foot-patrol and helicopter-assisted inspections, several grid owners, institutions, and researchers have investigated inspection robots for the automatic power line inspection and maintenance [3, 27, 34, 63, 67, 88]. The goal of mobile robots is to reduce cost (relative to aircraft-assisted inspection), enhance safety and reliably extend coverage. The automatic inspection solutions include automated helicopter-assisted inspection, flying inspection robots, climbing inspection robots [25, 51, 58] and hybrid inspection robots [2, 23]. Automated helicopter-assisted inspection face similar challenges than manned helicopter inspection such as obtaining high-quality images. Flying robots are operated by a foot-patrol agent. They can be design following UAV technology protocols and they present several advantages to helicopter inspection because they can be more compact, agile and fuel-efficient. However, flying robots face different challenges including control stability, automatic tracking, obstacle avoidance, communication and image acquisition among others. To increase the stability of robotic solutions, climbing robots have also been investigated by several researchers for many years. The robots are installed on the conductor and travel to monitor possible defects. A main challenge of climbing robot is the ability to cross obstacles along the line such as dampers and move from one span to another. These challenges increase the complexity of the robots design. Climbing robots also tend to have high power demand, short operation time and considerable weight. For instance, the LineScout robot developed by Hydro Quebec weighs about 120 kg [68] (Fig. 1.9) and the TI robot from EPRI is about 2 meters long [67] (Fig. 1.10).

1.3 Proposed solution

In light of the challenges presented by Stockbridge dampers and climbing inspection robots, in this thesis, we propose a mobile damping robot (MDR). The MDR combines the damping



Figure 1.9: Hydro Quebec Linescout inspection robot



Figure 1.10: The transmission line inspection robot developed by EPRI.

properties of our recent patented Aeolian vibration damper [15] as well as the mobility of climbing inspection robots. Combining the mobility of inspection robots with the vibration control characteristic of Aeolian vibration damper, the MDR can adapt to the changing wind characteristics and automatically re-position itself to antinodes. The idea of MDRs for vibration control is not new. For instance, Fei *et. al*, [30] discussed the advantages of using a MDR to critically suppress the vibrations of a work-piece during milling. Wang *et. al*, [86] studied the vibration suppression of a rigid body by using an absorber that slides across a groove. However, the application of a mobile device for WIV control has not been extensively reported in the literature.

1.3.1 Mechanical design and considerations

Figure 1.11 shows a detailed conceptual design of the MDR. The MDR is designed to be lightweight and more compact than the inspection robots currently in the field. The lightweight design feature is achieved because the activity of the MDR is limited to a single conductor span. Since most of the complexity of the climbing robots resides in their ability to cross obstacles and travel from one span to another, the MDR present a size and cost advantage. In Fig. 1.11-(a) we can see the overall conceptual design of the MDR with an in-span mass and a suspended mass. The design of the suspended mass is inspired by the 6R asymmetric Stockbridge [15] to maximize the number of resonant frequencies. Figure 1.11-(b) shows an exploded view of the MDR. The in-span mass consists of a clamping system as well as the necessary electronics to move the robot from one location to another. Clamping is essential because the robot needs to be stable and safely secured when it gets to a desired location. The in-span mass is connected to the messenger cable of the Stockbridge damper via a rigid frame.

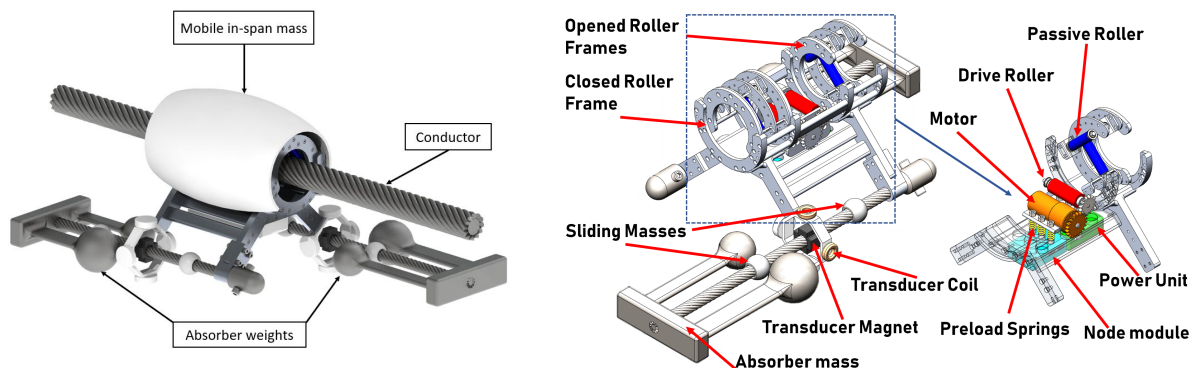


Figure 1.11: Conceptual design of the MDR attached to a power line cable.

1.3.2 Energy harvesting of WIV

To operate the locomotion and sensors of the MDR, it is essential to also consider an energy source. The goal of the proposed design is to have a stand-alone, self-powered device on the conductor. Relying on replaceable or rechargeable batteries, which are less economical [17], have limited life time, and are not environmental friendly, limits the autonomy of the MDR. A more appropriate solution can rely on energy harvesting and supply which is achieved conventionally via solar energy [77], electric-fields [1, 59, 62], and magnetic-fields [54, 90]. However, these sources of energy are not always available. A better path to energy harvesting would be to harvest energy generated by WIV, because WIV occur consistently. The transducer for WIV energy harvesting could be piezoelectric [28, 29, 38, 44, 66] or electromagnetic [21, 74, 79, 85, 94]. The selection of the transducer would be determined by the need of the MDR. For small-scale energy harvesting (W-mW) piezoelectric transducers are more suitable while for large-scale energy harvesting (W-kW), such as in civil structures and and shock absorbers [21, 48], electromagnetic transducers are more practical.

The performance of the harvester is strongly dependent on tunability. Power amplification can be realized when the harvester's natural frequency is tuned to the excitation frequency so as to create a resonant coupling. However, creating a resonant coupling is a challenge, particularly, for a vibration source with time-varying excitation frequency. Hence, a major drawback of WIV energy harvester is its narrow response bandwidth, making harvesters ineffective for most real life applications. To overcome this drawback, numerous investigators have explored techniques such as multiple resonators [72, 92], bistable systems [73, 91], or parametric resonance [20] to enhance the performance of the harvester. Another effective approach is to use passive self-tuning (PST) techniques for wideband energy harvesting [6, 57, 75]. PST can be realized using a slider along a continuum system (e.g. string, rod, or beam), in which the vibration of the continuum system drives the sliding mass. The

slider can cause the system to be off or in-resonance depending on the system parameters. This is because the sliding mass causes changes in the effective mass, and consequently in the system natural frequency. Experimental studies using a piezoelectric beam-slider system have revealed that self-tuning with a sliding mass can significantly improve the performance of a harvester [19, 45].

1.3.3 Modeling considerations

The Stockbridge Damper is a mechanical device that relies on nonlinear behavior. In this study, we limit the investigation to a simple linear model. To do so, the Stockbridge damper is reduced to an equivalent single degree of freedom (SDOF) system [9]. In this case, the parameters including the spring constant and the damping element can be tuned to match the resonant frequency of the cable. With this modeling simplification, we can study the performance of the MDR in terms of vibration control when the conductor is subject to an input excitation frequency that matches one of the conductor natural frequency.

Additionally, for energy harvesting purpose, we can also adapt the model by adding an electromagnetic shunt damper. Several researchers have studied the concept of shunt damping through a passive circuit to achieve simultaneously vibration control and energy harvesting. Passive circuit shunting for narrow-band reduction of resonant mechanical response was first demonstrated Forward *et. al.*, [32] in 1979. Further, Hagood and von Flotow [36] theoretically and experimentally proved that piezoelectric shunt with an RL circuit will act as a TMD. The use of shunt dampers using piezoelectric material and electromagnetic transducer is well-established in the literature [18, 31, 60, 89]. For both piezoelectric and electromagnetic designs, the resistive shunt exhibits viscous damping effects, while the inductor and the resistor introduce an electrical resonance, and acts like a mechanical vibration absorber.

Shunt dampers also provide vibration suppression for several energy levels and for a comparatively wider frequency range as compared to TMD [24, 87]. Further, it has been noted that using shunt dampers, it is possible to achieve both vibration control and energy harvesting. For instance, using the electromagnetic device in SD, some of the energy that was originally dissipated by the damping element of TMD, can be recovered electrically. With this objective, investigators have developed electromagnetic resonant shunt tuned mass dampers (ERS-TMD) [93]. In this study, we will consider the performance of the MDR with a simple equivalent SDOF Stockbridge damper as well as the performance of the MDR with an electromagnetic resonant shunt damper.

1.4 Objectives and Contributions of the Thesis

The objectives of the thesis are listed below:

1. Create a linear model of the MDR attached to a single conductor
2. Evaluate the implementation of a Proportional-Derivative controller for the horizontal dynamics of the MDR. Analytically determine the appropriate controller gains to meet specified performance criteria.
3. Compare the performance of the MDR to a SDOF fixed tuned mass damper in terms of vibration control of the conductor.
4. Assess the energy requirement of the MDR to travel to an antinode and determine if energy harvesting using an electromagnetic transducer can help cover some of the energy cost.
5. Compare the performance of the MDR with the energy harvesting MDR (EHMDR) in terms of vibration control.

6. Determine the key parameters that influence the performance of the MDR and the EHMDR.

The research accomplished in this thesis includes:

1. Linear modelling of the dynamics mobile damping robot with a Proportional-Derivative controller. The model also includes the incorporation of the electromagnetic transducer for energy harvesting purposes.
2. Proposed gain tuning rules and consideration for optimal control and energy specifications using the Linear-Quadratic-Regulator methodology.
3. Numerical results comparing the performance of the MDR, the fixed damper and the EHMDR in terms of vibration of WIV. The numerical examples also present energy harvesting potential for the EHMDR.

1.5 Thesis Organization

The introduction to this thesis is presented in Chapter 1. The governing equations of motion of the proposed MDR are derived using Hamilton's principle in Chapter 2. The energy requirement of the device is also addressed by considering the implementation of an electromagnetic shunt damping device. In this context, the mobile damping robot is reconsidered as a energy harvesting mobile damping robot (EHMDR). In Chapter 3, numerical analysis of the proposed design are carried out using MATLAB[®]. The numerical results are used to demonstrate the improvement in vibration suppression performance of the design when compared to the conventional fixed SDOF Stockbridge damper. Detailed parametric studies are also conducted to determine the role of different parameters that impact the performance of the robot. In Chapter 4, key insights of the results are discussed. Finally, some conclusions

are drawn in Chapter 5 and some future work ideas are presented.

Chapter 2

Vibration Suppression Control: Power lines

2.1 System Description and Modeling

This section presents the mathematical derivation of the mobile damping robot attached to a conductor. As mentioned previously, the proposed MDR is inspired by power lines inspection robots and asymmetric Stockbridge dampers. Figure 2.1 shows a simplified representation of the mobile device attached to the conductor. The conductor is modeled using Euler-Bernoulli beam theory with a length L , a mass per unit length m , a flexural rigidity EI and a pre-tension T . The Aeolian vibration damper of the mobile device is reduced to an equivalent single degree of freedom system [10], which has an in-span mass m_r , a suspended mass m_d , a

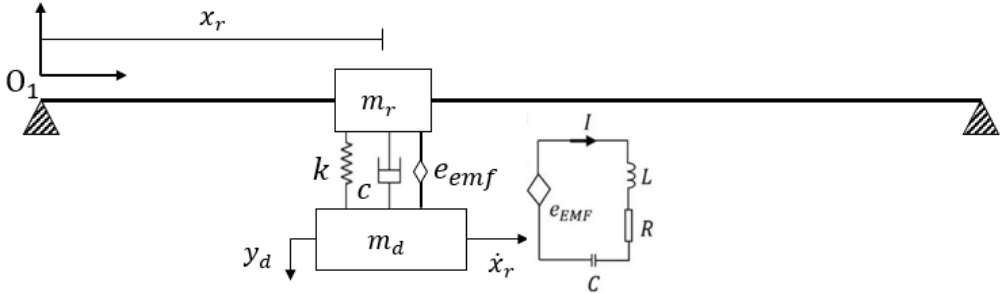


Figure 2.1: Schematic of the MDR on the cable

linear spring k , an equivalent damping coefficient c and horizontal velocity \dot{x}_r . Additionally, to provide an energy source to the robot we consider an electromagnetic device. The device is composed of an electromagnetic transducer, e_{emf} . The resistance, the inductance and the capacitance of the electrical circuit are denoted by R , L_i , and C , respectively. We also consider, the voltage constant and the force constant of the transducer denoted as k_v and k_f respectively.

2.1.1 Modeling the MDR

For simplicity, we first derive the model of the MDR without the electromagnetic device. The mathematical model of the system can be obtained by identifying the position vector of the beam, the in-span mass and the suspended absorber given as:

$$\mathbf{r}_b = x\mathbf{i} + y(x, t)\mathbf{j} \quad (2.1)$$

$$\mathbf{r}_r = x_r\mathbf{i} + y(x_r, t)\mathbf{j} \quad (2.2)$$

$$\mathbf{r}_d = x_r\mathbf{i} + y_d\mathbf{j} \quad (2.3)$$

where r_b , r_r and r_d represent the position of the beam, the in-span mass and the absorber, respectively. x and y represent the horizontal and vertical position across the beam. x_r is the location of the robot on the beam, and y_d is the vertical displacement of the damper.

The time derivatives of the position vectors are defined as:

$$\dot{\mathbf{r}}_b = \dot{y}(x, t)\mathbf{j} \quad (2.4)$$

$$\dot{\mathbf{r}}_r = \dot{x}_r\mathbf{i} + \left(\dot{y}(x_r, t) + y'(x_r, t)\dot{x}_r \right)\mathbf{j} \quad (2.5)$$

$$\dot{\mathbf{r}}_d = \dot{x}_r \mathbf{i} + \dot{y}_d \mathbf{j} \quad (2.6)$$

The definition of the velocity vectors can be used to formulate the kinetic energy of the system as:

$$E_k = E_{kb} + E_{kr} + E_{kd} \quad (2.7)$$

where E_{kb} , E_{kr} , and E_{kd} are the kinetic energy of the beam, the in-span mass, and the absorber, respectively. Each one of these energies may be expressed as:

$$E_{kb} = \frac{1}{2} m \int_0^L \left(\dot{y}(x, t) \right)^2 dx \quad (2.8)$$

$$E_{kr} = \frac{1}{2} m_r \left(\left(\dot{x}_r \right)^2 + \left(\dot{y}(x_r, t) + y'(x_r, t) \dot{x}_r \right)^2 \right) \quad (2.9)$$

$$E_{kd} = \frac{1}{2} m_d \left(\dot{x}_r^2 + \dot{y}_d^2 \right) \quad (2.10)$$

Similarly, the potential energy can be defined for each component of the system. The potential energy of the beam includes the restoring energy generated by the pre-tension and the material elastic properties. Consequently, the total potential energy can be summarized as:

$$V = \frac{1}{2} EI \int_0^L \left(y''(x, t) \right)^2 dx + \frac{1}{2} k \left(y(x_r, t) - y_d \right)^2 + \frac{1}{2} T \int_0^L \left(y'(x, t) \right)^2 dx \quad (2.11)$$

Using these energy expressions along with Hamilton's principle, the governing equation of motion of the cable can be expressed as:

$$EI y'''' + m \ddot{y} + T y'' = F(x, t) - (F_1 + F_2) D(x, t) \quad (2.12)$$

where $F(x, t)$ is the wind input force. This wind force is assumed to be uniformly distributed on the conductor and can be expressed as a time sinusoidal function following [35]:

$$F(t) = f_0 \sin(\omega_e t) \quad (2.13)$$

where f_0 is the amplitude of the wind force and ω_e represents the wind excitation frequency.

Since the mass of the mobile damping robot is small compared to the cable mass, the effect of Coriolis acceleration are neglected in F_1 and F_2 . F_1 , F_2 and $D(x,t)$ are given as:

$$F_1 = m_r \ddot{y} \quad (2.14)$$

$$F_2 = k(y - y_d) + c(\dot{y} - \dot{y}_d) \quad (2.15)$$

where the non-conservative force due to the damping element is considered.

$$D(x, t) = \delta(x - x_r) \quad (2.16)$$

The vertical displacement of the mass of the absorber can be expressed as:

$$m_d \ddot{y}_d - F_2 = 0 \quad (2.17)$$

In this work, the mobile robot actively tracks the antinode. Therefore, the equation of motion of the robot in the horizontal direction can be expressed as:

$$(m_d + m_r) \ddot{x}_r = F_c \quad (2.18)$$

where F_c represents a PD control force given as:

$$F_c = k_p(r - x_r) + k_d(-\dot{x}_r) \quad (2.19)$$

where k_p and k_d are the proportional and the derivative gains respectively. r represents the closest antinode location (i.e position target). Figure 2.2 shows the negative feedback control system diagram used to move the robot to the target antinode.

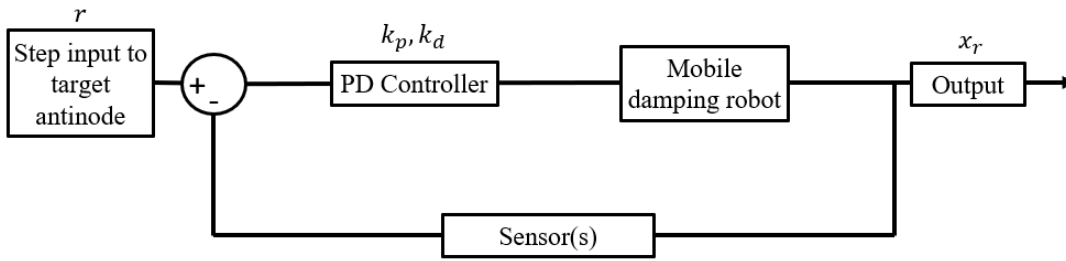


Figure 2.2: PD controller feedback loop that helps track the target antinode r .

To track the antinode, the MDR is also equipped with a wind sensor and an accelerometer. The wind sensor helps determine the Strouhal frequency expressed as:

$$f_s = 0.2 \frac{V_w}{D} \quad (2.20)$$

where f_s corresponds to the excitation frequency in Hz. V_w is the velocity of the wind and D represents the diameter of the conductor. Considering the case of resonance i.e., once the Strouhal frequency matches a conductor resonant frequency, the position of the antinode can be approximately determined. In this case, the controller generates a signal to the actuator to track the closest antinode. The accelerometer is used to measure the vibration of the conductor and help ensure that the average vibration across the cable is suppressed over time.

To reduce the number of parameters considered for the numerical analysis of the system, we

introduce the following nondimensional parameters:

$$\begin{aligned}
Y &= y/L; \xi = x/L; \xi_r = x_r/L; Y_d = y_d/L; p = r/L; \\
\tau &= \frac{t}{L^2} \sqrt{\frac{EI}{m}}; s^2 = \frac{TL^2}{EI}; C_d = cL \sqrt{\frac{1}{mEI}}; K = \frac{kL^3}{EI}; \\
f_0 &= \frac{FL^3}{EI}; M_r = \frac{m_r}{mL}; M_a = \frac{m_a}{mL}; K_p = \frac{k_p L^3}{EI}; K_d = \frac{k_d L}{\sqrt{mEI}};
\end{aligned} \tag{2.21}$$

where the frequency constant ω_p in the nondimensional time equation is given as:

$$\omega_p = \frac{1}{L^2} \sqrt{\frac{EI}{m}} \tag{2.22}$$

The equations of motion can thus be rewritten as:

$$Y'''' + \ddot{Y} - s^2 Y'' = f_0 \sin\left(\frac{\omega_i \tau}{\omega_p}\right) - (\bar{F}_1 + \bar{F}_2) \delta(\xi - \xi_r) \tag{2.23}$$

where \bar{F}_1 and \bar{F}_2 are given has:

$$\bar{F}_1 = M_r \ddot{Y} \tag{2.24}$$

$$\bar{F}_2 = K(Y - Y_d) + C_d(\dot{Y} - \dot{Y}_d) \tag{2.25}$$

The equation of motion of the robot is given as:

$$(M_r + M_d) \ddot{\xi}_r = K_p(p - \xi_r) + K_d(-\dot{\xi}_r) \tag{2.26}$$

The equation of motion of the suspended mass is given as:

$$M_d \ddot{Y}_d = K(Y - Y_d) + C_d(\dot{Y} - \dot{Y}_d) \quad (2.27)$$

In order to discretize the partial differential equation of the system into a system of ordinary differential equations, the solution can be expressed using the Galerkin decomposition method as:

$$Y(\xi, \tau) = \sum_{r=1}^{\infty} \Phi_r(\xi) A_r(\tau) \quad (2.28)$$

where $A_r(\tau)$ are the normalized time functions of the transverse displacement, and $\Phi_r(\xi)$ are the normalized eigenfunctions (mode shapes). The eigenfunctions are chosen as the mode shapes of a simply supported beam with tension ([16]) as:

$$\Phi_r(\xi) = \sqrt{2} \sin \left(\left(\sqrt{\frac{s^2}{2} + \sqrt{\frac{s^4}{4} + \omega_r^2}} \right) \xi \right) \quad (2.29)$$

where the natural frequencies of the bare beam are given by

$$\omega_r = \pi^2 \sqrt{r^4 + \frac{r^2 s^2}{\pi^2}} \quad (2.30)$$

Substituting Equation 2.28, into Equation 2.12, multiplying by $\Phi_i(\xi)$, integrating over the length of the beam, and applying the orthogonality condition yields

$$\begin{aligned} & \ddot{A}_p(\tau) + M_r \left[\sum_{r=1}^{\infty} \ddot{A}_r(\tau) \Phi_r(d) \right] H_p(\tau) + 2\zeta \omega_p \dot{A}_p(\tau) + \omega_p^2 A_p(\tau) \\ & + \left\{ K \left[\sum_{r=1}^{\infty} A_r(\tau) \Phi_r(d) - Y_d(\tau) \right] + C_d \left[\sum_{r=1}^{\infty} \dot{A}_r(\tau) \Phi_r(d) - \dot{Y}_d(\tau) \right] \right\} H_p(\tau) = S_p(\tau) \quad (2.31) \end{aligned}$$

Similarly, Eq. 2.17 and Eq. 2.19 yield

$$(M_d + M_r)\ddot{\xi}_r(\tau) = K_p(p - \xi_r(\tau)) + K_d(\dot{p} - \dot{\xi}_r(\tau)) \quad (2.32)$$

$$M_d\ddot{Y}_d(\tau) - K \left[\sum_{r=1}^{\infty} A_r(\tau)\Phi_r(d) - Y_d(\tau) \right] + C_d \left[\sum_{r=1}^{\infty} \dot{A}_r(\tau)\Phi_r(d) - \dot{Y}_d(\tau) \right] = 0 \quad (2.33)$$

where $S_p(t)$ and $H_p(t)$ can be defined as:

$$S_p(\tau) = \int_0^1 \Phi_r(\xi)F(\xi, \tau)d\xi, r = 1, 2, \dots \quad (2.34)$$

$$H_p(\tau) = \int_0^1 \Phi_r(\xi)\delta(\xi - \xi_r)d\xi, r = 1, 2, \dots \quad (2.35)$$

and d is the position of the damper, which corresponds to ξ_r for the MDR.

To determine the performance of the mobile damping robot, the normalized energy dissipated is defined as follows:

$$\bar{E}_{disp} = \int_0^{\tau} c \left[\dot{Y}_d(\tau) - \sum_{r=0}^{\infty} \dot{A}_r(\tau)\Phi(v_d\tau) \right]^2 d\tau \quad (2.36)$$

The efficiency of the absorber can be obtained as in [71]:

$$\eta = \frac{\bar{E}_{disp}}{\bar{W}} \quad (2.37)$$

where \bar{W} is the normalized work due to the external force, and it can be obtained as:

$$\bar{W} = \int_0^\tau \int_0^L F(\xi, \tau) \Phi(\xi) \dot{A}(\tau) d\xi d\tau \quad (2.38)$$

From this expression of work, we can established the normalized power transferred to the cable across the normalized length as:

$$\bar{P}(\xi) = \int_0^\tau F(\xi, \tau) \Phi(\xi) \dot{A}(\tau) d\tau \quad (2.39)$$

It is also useful to define the normalized energy required to operate the robot as follow:

$$\bar{E}_c = \int_0^\tau F_c \dot{\xi}_r \quad (2.40)$$

2.1.2 Modeling the MDR with the energy harvester

The electromagnetic dynamics can be added to the previous model using Newton's method.

In Eqs. 2.12 and 2.17 F_2 is redefined as:

$$F_2 = k(y - y_d) + c(\dot{y} - \dot{y}_d) + k_f \dot{q} \quad (2.41)$$

where \dot{q} represents the current variation in the electromagnetic circuit.

In addition, the dynamics of the electromagnetic circuit is summarized in the following equation:

$$L_i \ddot{q} - k_v(\dot{y} - \dot{y}_d) + R\dot{q} + \frac{1}{C}q = 0 \quad (2.42)$$

we introduce the following nondimensional parameters for the electromagnetic device:

$$Q = \frac{q}{q_0}; K_f = \frac{k_f q_0}{\sqrt{m EI}}; K_v = \frac{k_v L}{L \omega_p q_0}; \bar{R} = \frac{R}{L \omega_p}; \bar{C} = \frac{1}{CL \omega_p^2} \quad (2.43)$$

By substituting the nondimensional parameters in the previous equation we obtain:

$$\bar{F}_2 = K(Y - Y_d) + K_f \dot{Q} + C_d(\dot{Y} - \dot{Y}_d) \quad (2.44)$$

$$\ddot{Q} - K_v(\dot{Y} - \dot{Y}_d) + \bar{R}\dot{Q} + \bar{C}Q = 0 \quad (2.45)$$

In terms of energy computation, we consider the power and the energy harvested by the device for later use. We define these terms as:

$$\bar{P}_{har}(\tau) = \bar{R}\dot{Q}^2(\tau) \quad (2.46)$$

$$\bar{E}_{har} = \int_0^\tau \bar{R}\dot{Q}^2(\tau) d\tau \quad (2.47)$$

2.2 Validation using the Harmonic Balance method

The system that we consider is a continuous system with a dynamical device attached to it. The model described below can be made as accurate we wish using as many modes of vibrations as possible. However, for the sake of validating the model, we simplify the continuous system to a single mode system. In this case, it is possible to compare the numerical simulations to the analytical results obtained using the harmonic balance method (HBM). To get the analytical solution, we assume the time function of the cable (single

mode), the suspended damper mass and the variation in charge to be defined as:

$$A(\tau) = A_{s0} + A_s \cos(\omega\tau) + B_s \sin(\omega\tau), \quad (2.48a)$$

$$Y_d = A_{t0} + A_t \cos(\omega\tau) + B_t \sin(\omega\tau), \quad (2.48b)$$

$$Q = A_{i0} + A_i \cos(\omega\tau) + B_i \sin(\omega\tau). \quad (2.48c)$$

These assumed solutions are substituted in Eqs. 2.23, 2.27 and 2.45. By collecting the coefficients of the cosine and sine terms for each harmonics along with constant terms, we obtain six linear algebraic equations denoted as $z_1 - z_6$ which are described as:

$$\begin{aligned} z_1 = & (-B_t)K\Phi + B_sK\Phi^2 - A_tC_d\Phi\omega + A_iK_f\Phi\omega \\ & + Asc\Phi^2\omega - B_s\omega^2 - B_sM_r\Phi^2\omega^2 + B_s\omega_r^2, \end{aligned} \quad (2.49a)$$

$$z_2 = B_tK - B_sK\Phi + A_tC_d\omega - A_iK_f\omega - A_sC_d\Phi\omega - B_tM_a\omega^2, \quad (2.49b)$$

$$z_3 = B_i\bar{C} + A_tK_v\omega - A_sK_v\Phi\omega + A_i\bar{R}\omega - Bi\omega^2, \quad (2.49c)$$

$$\begin{aligned} z_4 = & (-A_t)K\Phi + A_sK\Phi^2 - f_0 \int_0^1 \Phi + B_tC_d\Phi\omega \\ & - B_iK_f\Phi\omega - B_sC\Phi^2\omega - A_s\omega^2 - A_sM_r\Phi^2\omega^2 + A_s\omega_r^2, \end{aligned} \quad (2.49d)$$

$$z_5 = A_tK - A_sK\Phi - B_tC_d\omega + BiK_f\omega + B_sC_d\Phi\omega - A_tM_a\omega^2, \quad (2.49e)$$

$$z_6 = A_i\bar{C} - B_tK_v\omega + B_sK_v\Phi\omega - B_i\bar{R}\omega - A_i\omega^2. \quad (2.49f)$$

To solve these linear algebraic simultaneous equations, we use the fixed arc-length contin-

uation scheme developed in [84]. With this methodology, it is possible to compare the frequency response of the system obtained using the harmonic balance against the numerical simulations. The validation will be discussed in the following chapter.

Chapter 3

Results

In this section, we start with validating our analytical results obtained using the HBM to establish their accuracy. Then, the proposed MDR is compared to the conventional FTMD in terms of vibration control. Further, the energy requirement of the PD controller is assessed. Some analysis is provided for considering an electromagnetic device for energy harvesting purposes (EHMDR). Finally, different parametric analysis are conducted for optimal control and optimal energy harvesting.

3.1 Validation and numerical considerations

The model presented in Chapter 2 can be validated by comparing the numerical results of the MATLAB function 'ode45' to the analytical results of the harmonic balance method. The comparison is done for the fundamental frequency of the system. The problem is simplified by fixing the position of the device on the cable. Figure 3.1 shows that there an excellent agreement between the numerical and the analytical results with a maximum error of 0.3%. Because we explore more than one mode of vibration, the numerical approach will be used in the subsequent analysis unless otherwise noted.

For the numerical approach, it is necessary to determine the number of terms in the Galerkin approach required to get an acceptable approximate solution for the displacement of the cable 2.28. To achieve this goal, we simulated the vibration of the bare cable for an input excitation

Table 3.1: Parameters of the conductor and the applied load

$L(m)$	$m(\text{kg}/m)$	$T(N)$	$EI(N.m^2)$	$\omega_n(\text{rad}/s)$	$f_0(N/m)$
27.25	1.6286	27840	1602	ω_n	See Eq.

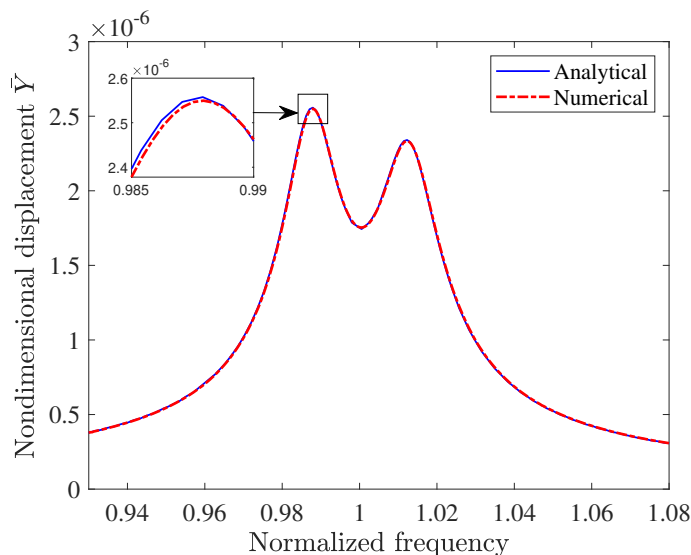


Figure 3.1: A comparison between analytical and numerical simulation for the fixed damper.

matching ω_3 . We then recorded the maximum displacement of the cable at the midspan as presented in Fig. 3.2-(a) for five, ten, fifteen, twenty and twenty-five and thirty terms. The results show that as we increase the number of terms from five to ten terms, there is a significant drop in the displacement value. As we increase, the number of terms further, we observe that the maximum displacement value remains relatively constant. Therefore, we can consider at least ten terms for accurate results.

Furthermore, we can also evaluate the number of terms required for numerical simulations by studying the maximum displacement of the cable when attached to a fixed damper. Figure 3.2-(b) considers the normalized displacement of the cable with a fixed damper attached. In this case, we can see a significant jump in the displacement of the cable when increasing the number of terms from five to ten terms. In this case, the relative percent difference in values

is close to 20%. However, as we continue to increase the number of terms in the simulation, the relative difference in value decreases significantly to 6.7% (10 to 15), 0.9% (15 to 20), 0.5% (20 to 25), and 0.8% (25 to 30). Therefore, the results show that past twenty terms, the difference in the normalized maximum displacement is relatively constant. Consequently, to ensure a satisfying approximations to the dynamics of the cable and the dampers, in the remainder of the analysis we will consider twenty terms.

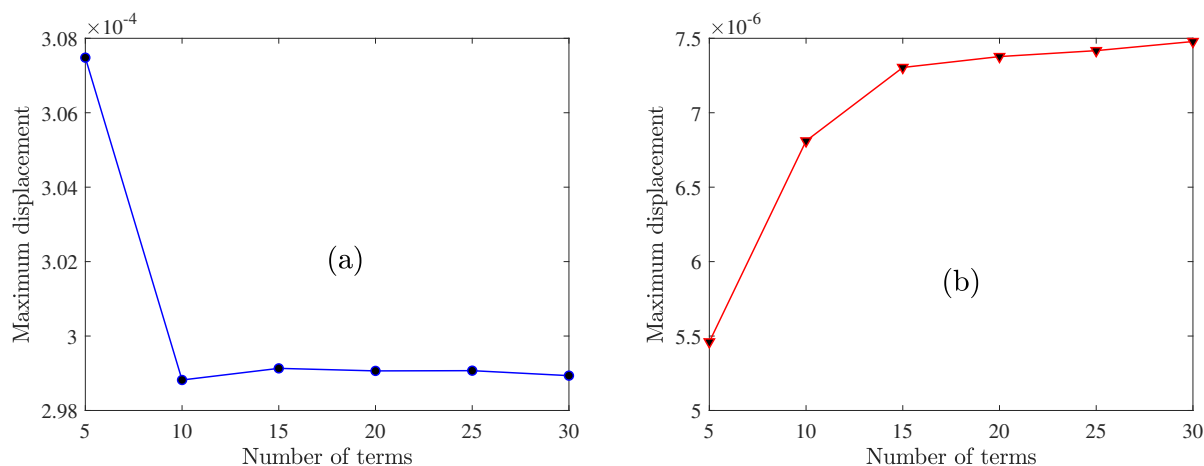


Figure 3.2: Determining the number of modes required for the numerical simulation. Figure 3.2-(a) considers the vibration of the bare beam while (b) consider the vibration of the beam with a fixed damper.

3.2 Mobile damping robot performance

3.2.1 Proportional and derivative gain for optimal control

Having validated the mathematical model, we provide a presentation of the PD controller used for the proposed MDR. The robot relies on a control scheme to move to the antinode and help mitigate the vibration of the cable. To determine the proportional and derivative gains for optimal control, the control requirements for the design need to be specified. The

mobile robot is required to reach the antinode in a reasonable amount of time and hence the rise time is a key design parameter. Indeed, the faster the robot reaches the antinode, the quicker the vibration of the cable is reduced. Additionally, we also desire to minimize the steady state error to ensure that the robot reaches and stays at the antinode. With these requirements in mind, we can iterate the values of k_p and k_d . Figure 3.3 shows the impact of varying the values of k_p and k_d . The results show that when we only have a proportional gain (i.e, $k_d = 0$, we are able to travel towards the antinode but we can not achieve zero steady state error. Also, when we set the proportional gain to be zero we can not follow the target and we stay at the original location of the damper. The results also show that when we have a proportional gain 2 times larger than the derivative, the steady state is minimized and we only have negligible percent overshoot. When the derivative is set to be larger, we get a better response overall with no steady state error and no percent overshoot. These observation gives us the general ideas about how to select the gains. However, to deal with input demand requirements, it will require multiple trial and errors to optimized the gains.

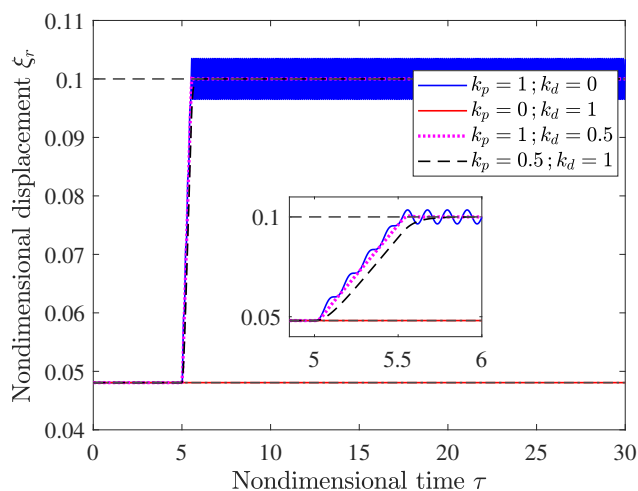


Figure 3.3: Determining the values of k_p and k_d for optimal control

To resolve this trial and error issue in optimizing the control parameters, we can use a control scheme such as the Linear-Quadratic Regulator (LQR) function in MATLAB to determine

the appropriate value of k_p and k_d . To use the LQR function, we use Eq. 2.18 to determine the state-space arrangement for the error given as:

$$\dot{e} = \begin{bmatrix} 0 & 1 \\ 0 & 0 \end{bmatrix} e + \begin{bmatrix} 0 \\ \frac{-1}{m_r+m_d} \end{bmatrix} F_c$$

where e is the error given as $e=r - \xi_r$, and e is the error state vector. The state matrix A and the input matrix B are selected as input to the LQR function. We also determine the Q matrix to assign the weight of importance for the error in position and the error in velocity of the robot. We also determine the R matrix to assign the weight of the input force. LQR solves $F_c = -K e$ where $K = [-k_p - k_d]$ to minimize its cost function. The relative ratio of the R to Q will determine if the cost function focuses on reaching the position with any amount of input force necessary ($Q \gg R$) or if minimizing the energy effort is more important ($R \gg Q$). Using the LQR scheme, we find that for optimal control $k_d > k_p$. Figure 3.4 shows the response of the robot when the input excitation matches the cable natural frequency ω_5 . The results show that the robot reaches the target antinode with no overshoot and no steady state error within 18 normalized time steps. The appropriate values of k_p and k_d found using LQR are used in the subsequent sections.

3.2.2 Comparing the fixed absorber to the MDR

In this section, we compare the performance of the fixed damper to the proposed mobile damping robot. To achieve this task, we excite the cable at a resonant frequency and we observe the performance of each device. The fixed damper location on the cable is optimized using observations in the literature. For instance, in Barry *et. al*, [9], the analysis shows that the damper should be placed within the vibrating loop corresponding to the highest

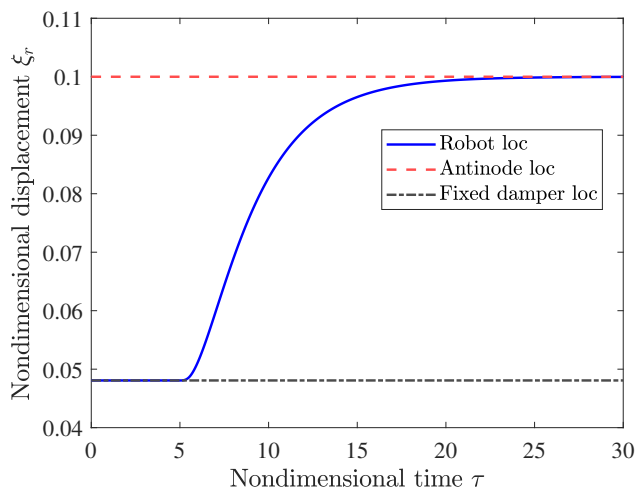


Figure 3.4: Determining the values of k_p and k_d for optimal control

excitation frequency. The highest frequency is related to the highest speed through Eq. 2.20. For Aeolian vibration, the highest wind speed is near 7 m/s . In this case, it is advised to place the fixed damper between 85% and 90% of the vibrating loop. This consideration is taken into account in the following analysis to ensure a fair comparison between the fixed damper and mobile damper. For the selected 795 Drake ACSR conductor, a 50 Hz frequency corresponding to the highest wind speed 7 m/s is obtained using Eq. 2.20. Following this procedure The fixed damper is placed at a normalized location of 0.0481 following [9].

Aeolian vibration frequencies for the selected cable range from 3.57 Hz to 50 Hz (0.5 m/s to 7 m/s). These frequencies correspond to the mode shape range of ω_2 - ω_{18} . The frequency response of the cable with and without a damper can be generated as in Fig. 3.5. The results from this frequency map is that when the robot is within a vibrating loop we can see a lot of oscillation. In this situation, the damper can be effectively used for vibration control. Indeed, Fig. 3.5-(b) a 20 dB drop in vibration magnitude when the robot is place within a vibration loop. However, when the robot falls on a node, there is no motion. This incident can cause grave damage to the cable. Furthermore, it is also important to note that

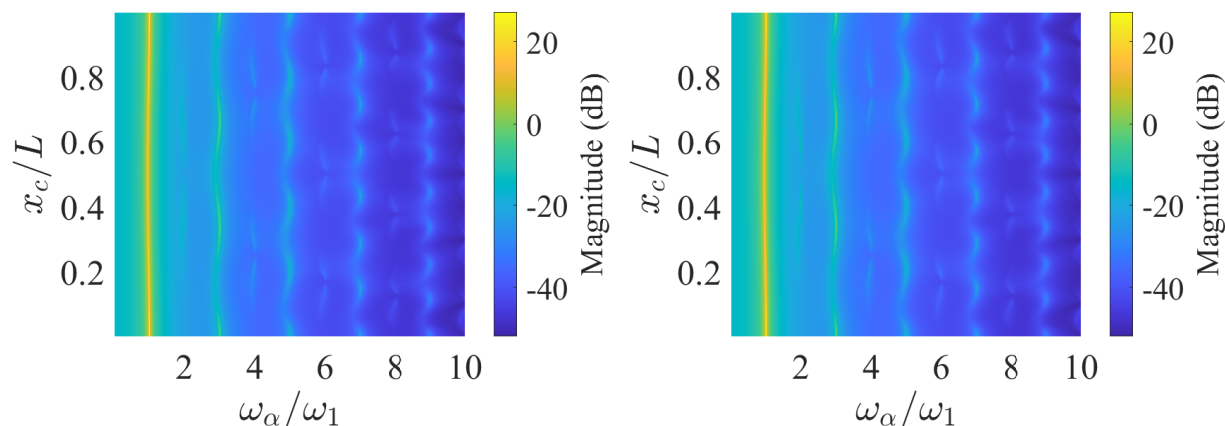


Figure 3.5: Frequency response of the cable and the robot along the span. Figure 3.5-(a) shows the transmissibility of the cable as a function of the normalized frequency. Figure 3.5-(b) shows the transmissibility of the cable with a damper attached as a function of the normalized frequency.

odd modes show significant vibration levels while even modes show minimal vibration even though the system is excited at resonance. This observation can be justified by the fact that the cable even modes are destructive. For this reason, most of the following analysis focuses on odd modes.

Now that we have an understanding of the cable vibration levels, we can compare the fixed damper to the mobile damper in terms of vibration control. It is necessary to compare the overall impact of the damper on the vibration of the cable across the length. To do so, we can do so using different methods. One method focuses on the time response of the system with the dampers. Because the time function of the Galerkin decomposition is directly numerically integrated, we can get some insight of the response of the cable with and without dampers. Figure 3.6-(a) shows the time function maximum amplitude for each mode of the cable when the cable is excited at the fundamental frequency. We can see that when the cable is excited with no damper, the time function of the first mode dominates the motion and is significantly larger than the other modes. Attaching the dampers to the

cable causes a significant decrease in the first time function amplitude. Figure 3.6-(b) shows the the time response for all damping conditions. We can see from the Figure that the cable with no damper goes into resonance as expected. We also observe that the displacement of the cable with the dampers is at least two orders of magnitude smaller in Fig.3.6-(c). Additionally, Fig. 3.6-(c) shows that the MDR can further reduce the vibration of the cable by moving towards the antinode. Overall, the results show that adding the dampers help vibration mitigation. The results also show that the MDR offers additional vibration efficiency.

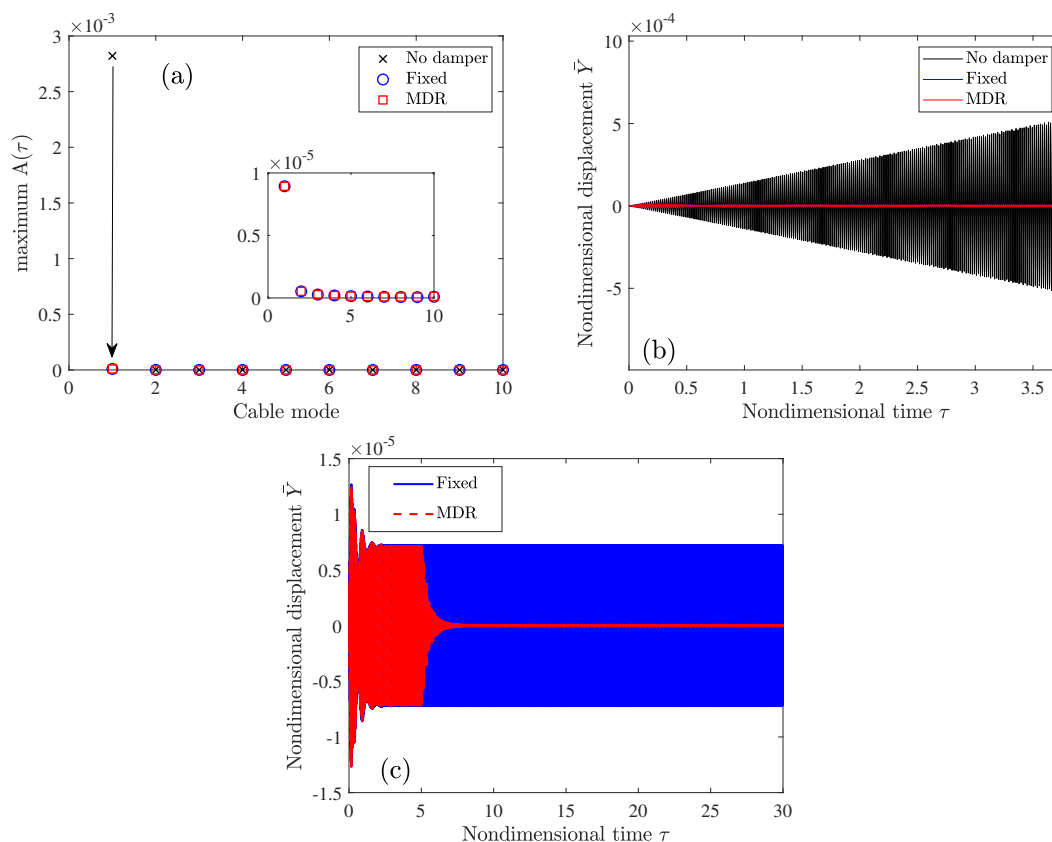


Figure 3.6: Time functions and time response of the cable comparing the performance of the fixed damper against the MDR for $\omega_e = \omega_1$.

We can also study specifically the impact the input force on the cable by determining the amount of power transferred to each point along the conductor. To do so, we present Figures

3.7-(a)-(d) which show the normalized power as a function of the normalized length for ω_3 , ω_9 , ω_{13} and ω_{17} . As stated before, we focus on odd modes because even modes are destructive and cause minimal vibration of the cable. Figures 3.8-(a)-(d) shows for the corresponding frequencies, the final location of the fixed and the mobile damper on the cable across the normalized length. The location of each damper is displayed on the mode shape of the input frequency. The results show that as the excitation frequency increases, the location of the fixed damper changes relative to the location of the antinode of the vibration loop. The results also show that overall the performance of the MDR is superior when the fixed damper is further away from the antinode (i.e., ω_3, ω_{17}). However, when the fixed damper location is very close to an antinode, the performance of the fixed damper and the mobile damping robot is comparable (i.e., ω_9, ω_{13}).

It is also useful to evaluate the performance of the fixed damper against the mobile damper in terms of vibration control using the concept of work define in Eq. 2.38. Figure 3.9 shows the normalized work done on the cable as a function of the odd excitation frequencies. The results show that overall, the work done on the cable with the fixed damper is superior to the work done on the cable with the MDR. Between ω_3 - ω_7 , it is clear that the MDR performs better than the fixed damper by minimizing the work done by the input frequency. The same observation can be done for ω_{13} - ω_{17} . Between ω_9 - ω_{11} , the fixed damper matches the antinode location. In this case, the MDR does not move. Therefore, the performances of the dampers are similar and optimal.

We have shown that the mobile damper is superior in most cases to the fixed damper as it reduces the amount of work done on the cable. Using the total amount of work done for each damper, it is also possible to determine the efficiency of the devices. The efficiency of the absorber relative the work done on the cable is presented as Eq. 2.37. However, this formula is relative to each damper. To allow a more holistic comparison, it is necessary to

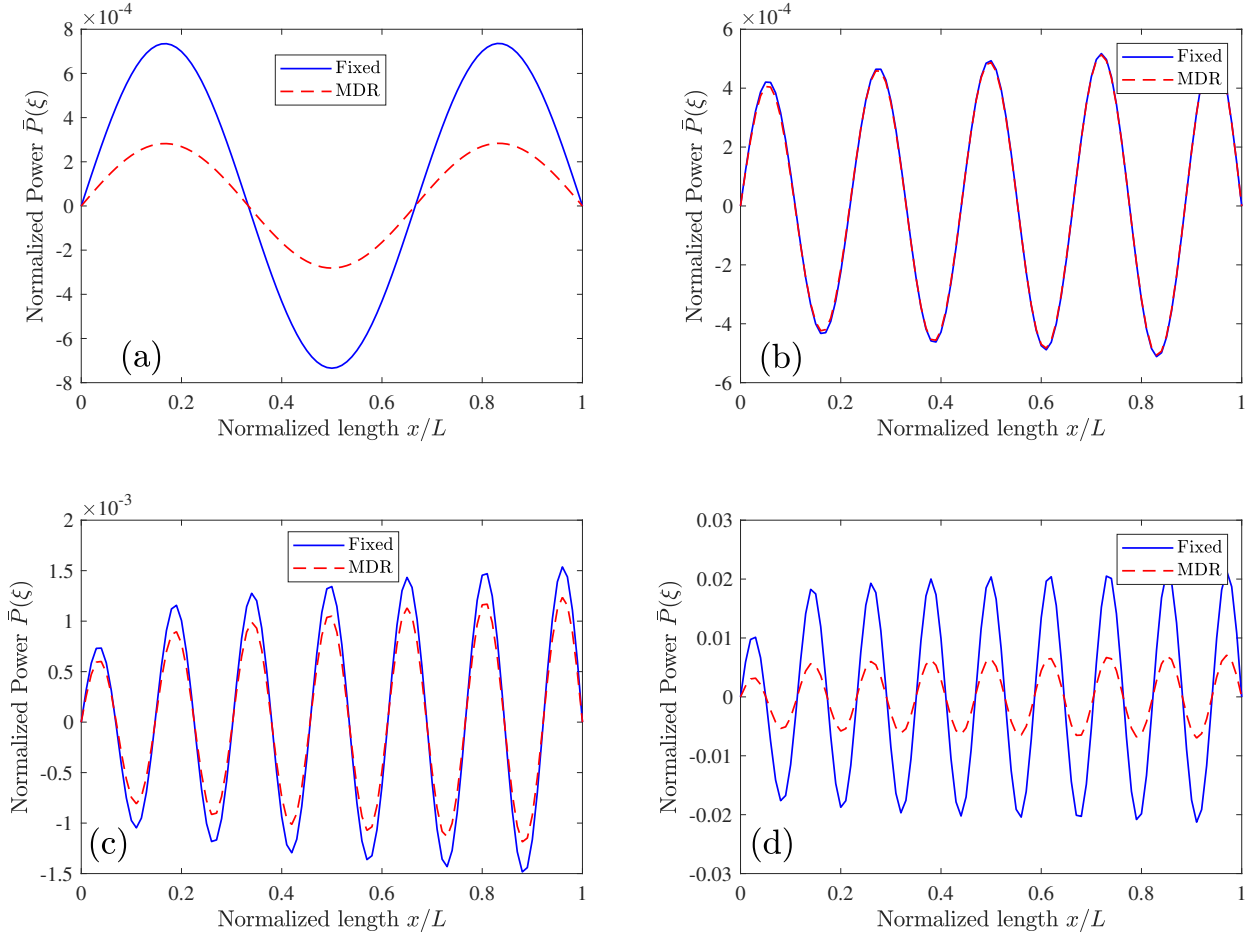


Figure 3.7: A comparison of the vibration control performance of the fixed damper and the proposed MDR for (a) ω_3 , (b) ω_9 , (c) ω_{13} and (d) ω_{17} .

compare the performance of each damper relative to the same work input to the system. To do so we introduce the following Equations:

$$\eta_i = \frac{\bar{W}_o - \bar{W}_i}{\bar{W}_o} \quad (3.1)$$

$$\eta_i = \frac{\bar{W}_s - \bar{W}_i}{\bar{W}_s} \quad (3.2)$$

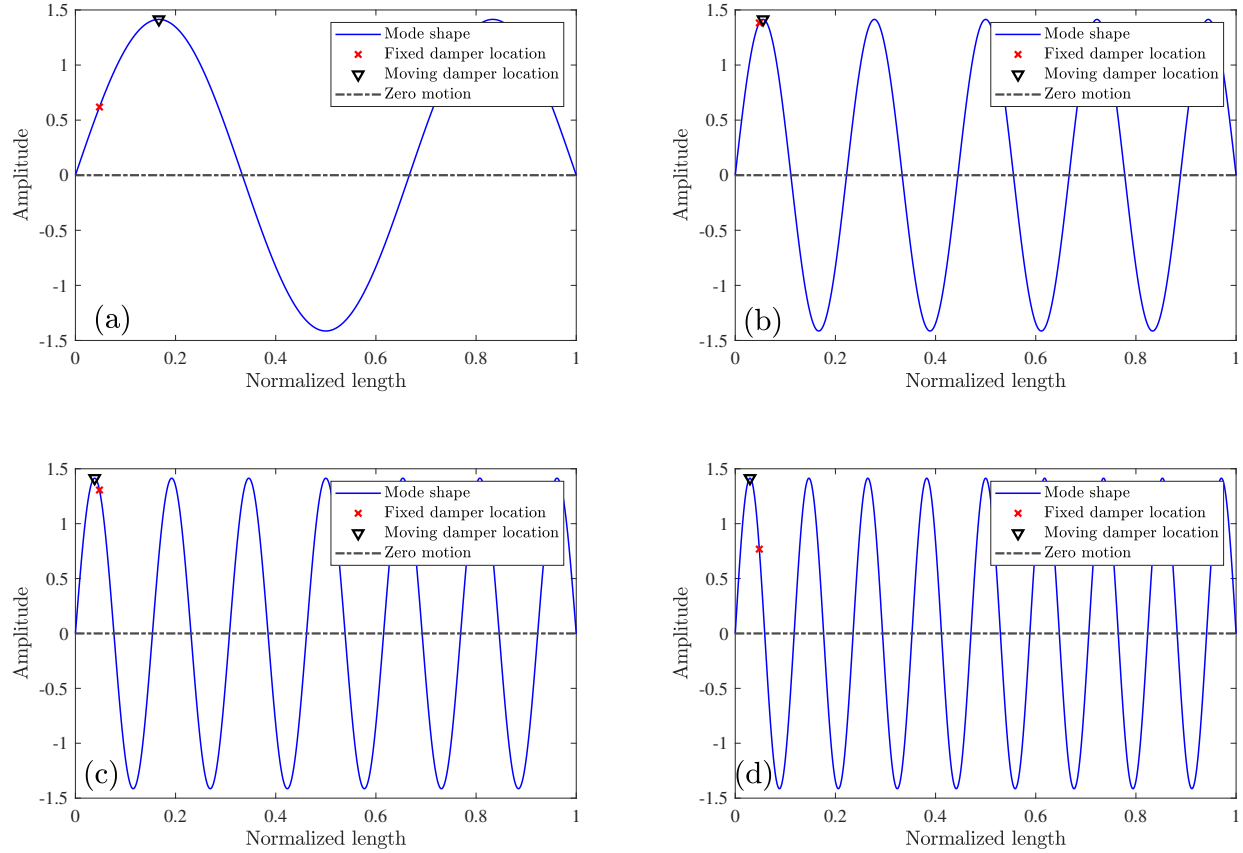


Figure 3.8: Final location of the fixed damper and the mobile damper for varying input excitation.

where \bar{W}_o represents the total amount of work done on the cable without any damper at resonance . Equation 3.1 is used for the fixed damper and mobile damper as long as the work done by the fixed damper and the mobile damper \bar{W}_i is smaller than \bar{W}_o . If the work done by the fixed damper \bar{W}_f or the mobile damper \bar{W}_m noted as \bar{W}_i is greater than \bar{W}_o , that work is used at the reference \bar{W}_s to calculate the efficiency. Using these Equations, it is possible to assess the efficiency of each damper for varying frequencies. Figure 3.10 shows the efficiency of each device. The results show that the efficiency for both devices is superior to 95% in general. However, for all frequencies, the MDR performs as well or better than the

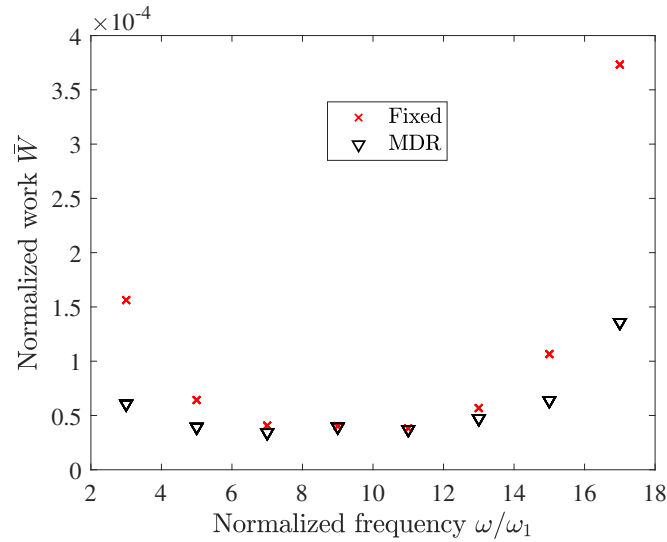


Figure 3.9: Comparing the normalized work done on the cable for the fixed damper and the MDR for varying normalized frequency.

fixed damper. We observe that the efficiency is identical for frequencies where the location of the fixed damper matches an antinode.

We have established that the performance of the mobile damper is superior or comparable to the performance of the fixed damper, as long as the dampers are within the vibrating loop. We further our investigation by assessing the worst case scenario in which the fixed damper coincide with a node. We can assess the performance by looking at the time response of the cable as in Fig. 3.11-(a). The results show that the cable with the fixed damper goes into resonance. Indeed, in this case, the damper is incapable of transferring energy to its suspended mass. The displacement of the cable with the fixed damper is worse than the displacement of the cable with no damper at all. This shows how critical the position of the damper is. For the mobile damping robot, because we are able to move to the antinode, the displacement of the robot gets reduced to nearly zero. Looking at the steady response (Fig. 3.11-(b)). Shows that the mobile damping robot has a superior performance in terms of vibration control.

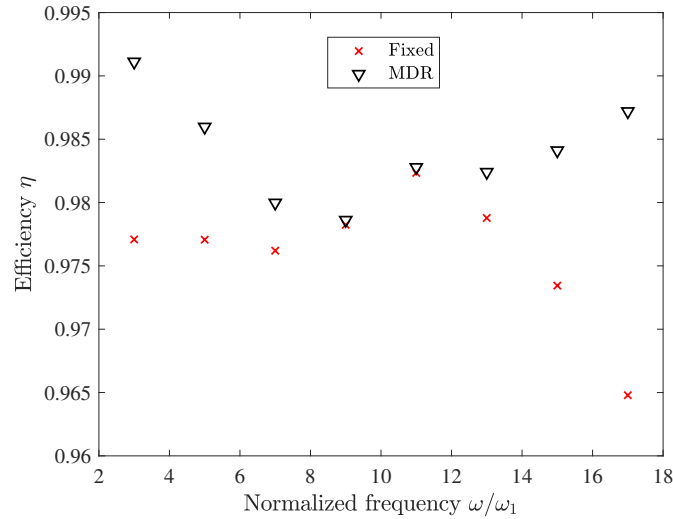


Figure 3.10: Comparing the efficiency of the fixed damper to the MDR for varying normalized frequencies.

We also study this nodal case in terms of the normalized power at each location across the cable and in terms of efficiency. Figures 3.12-(a)-(b) show the normalized power as a function of the normalized length across the cable for ω_3 . In Fig. 3.12-(a), the dampers are initially placed at a node, while in Fig. 3.12-(b), the dampers are initially placed at the optimal location of the fixed damper 0.0481 as in Fig. 3.7-(a). In both figures, the normalized power across the normalized length of the cable with no damper is also presented. Figure 3.12-(c) shows an overview of the performance of each damper in terms of the efficiency across a vibrating loop of the cable for ω_3 . The results show that as long as the fixed damper is placed within the vibrating loop it performs relatively well (i.e., $\eta > 60\%$). The results also show that the mobile damping robot in all cases outperforms the fixed damper with at least 80% efficiency for all initial locations across the vibration loop. Adding the dampers shows a significant value in mitigating vibration. However, when the fixed damper coincides with a node, the cable is subject to more vibrations than when no damper is attached. In this case, the MDR can address this issue by re-adjusting itself at the antinode. It prevents the significant damages that are caused by staying at the node.

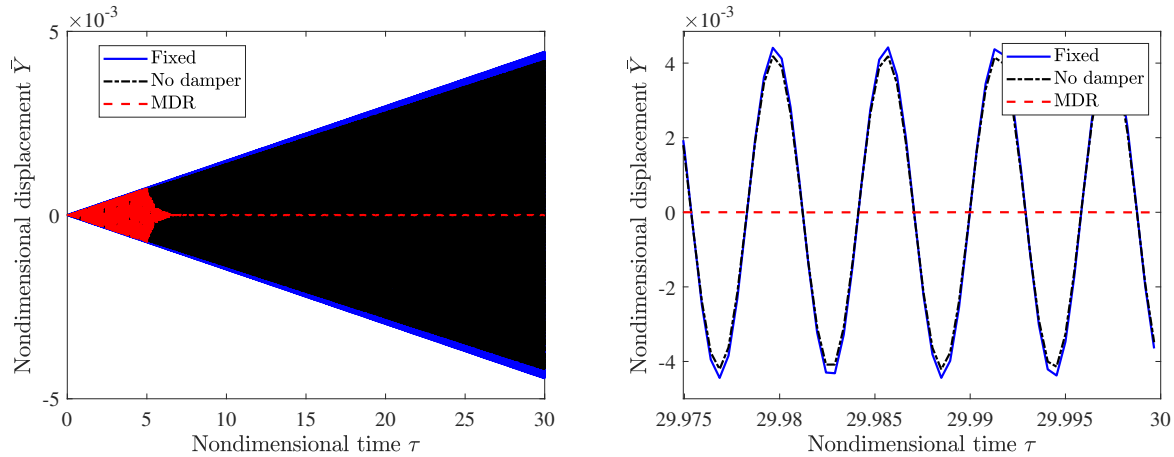


Figure 3.11: Time response for different damping conditions when the initial location of the dampers coincide with a node.

We have established that the mobile damping robot is superior to the fixed damper especially when the fixed damper coincide with a node. We can also assess the performance of the dampers in terms of the normalized frequency. Figure 3.13 shows the maximum normalized displacement of the cable as a function of normalized frequency. The cable is excited at frequency near the fundamental frequency ω_1 . The fixed damper is installed at its optimal location i.e, 0.0481. The results show that adding the dampers significantly reduce the displacement of the cable at resonance. We also note that the MDR is able to reduce the vibration to nearly zero because it moves towards the antinode. Additionally, the MDR has a wider range of frequency where it can exert vibration control. In Figure 3.13-(b), we notice that the MDR frequency response has two large vibration peaks when compared to the fixed damper frequency response. To resolve this issue, we can limit the movement of the MDR to frequencies, where the vibration of the cable is minimized when the robot goes to the mid-span (antinode) as shown in Fig. 3.13-(b).

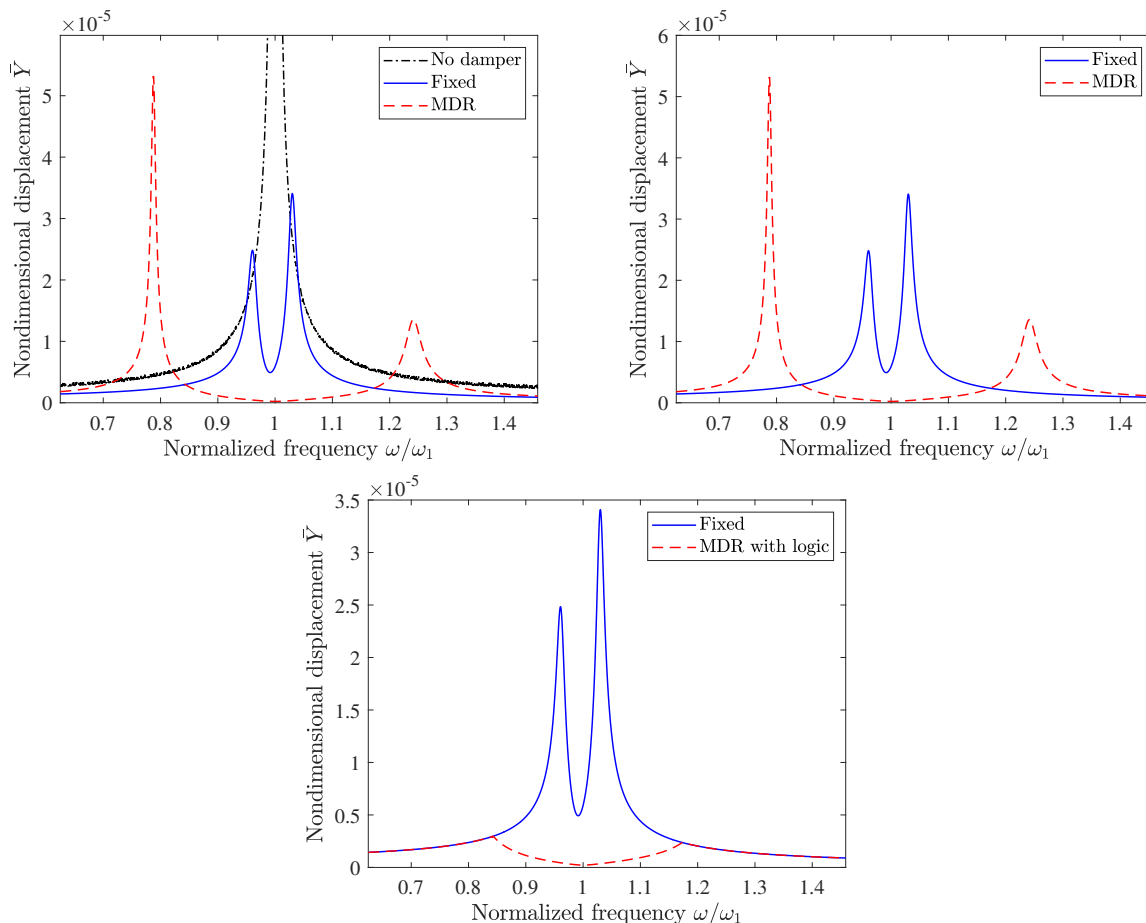


Figure 3.13: Comparing the steady state normalized displacement of the cable for each damping condition for varying normalized frequencies.

mobile damper for optimal vibration mitigation. In this effort, we present Fig. 3.14-(a)-(c). Figure 3.14-(a) shows the normalized power across the normalized length of the cable for ω_3 . Figure 3.14-(b) shows the normalized work done on the cable as a function of α . We define α as the percent of the in-span mass that represent the total mass of the mobile device $m_T = m_r + m_a$. In this case, we also define $1 - \alpha$ as the mass percent of the suspended damper relative to the total mass m_T . Using the nondimensional parameters we can also define $\bar{m}_T = \bar{M}_r + \bar{M}_a$. The results show that changing the relative mass of the in-span mass tend to increase the amount of work done on the cable while increasing the suspended mass improves the performance of the MDR in terms of vibration reduction. The efficiency

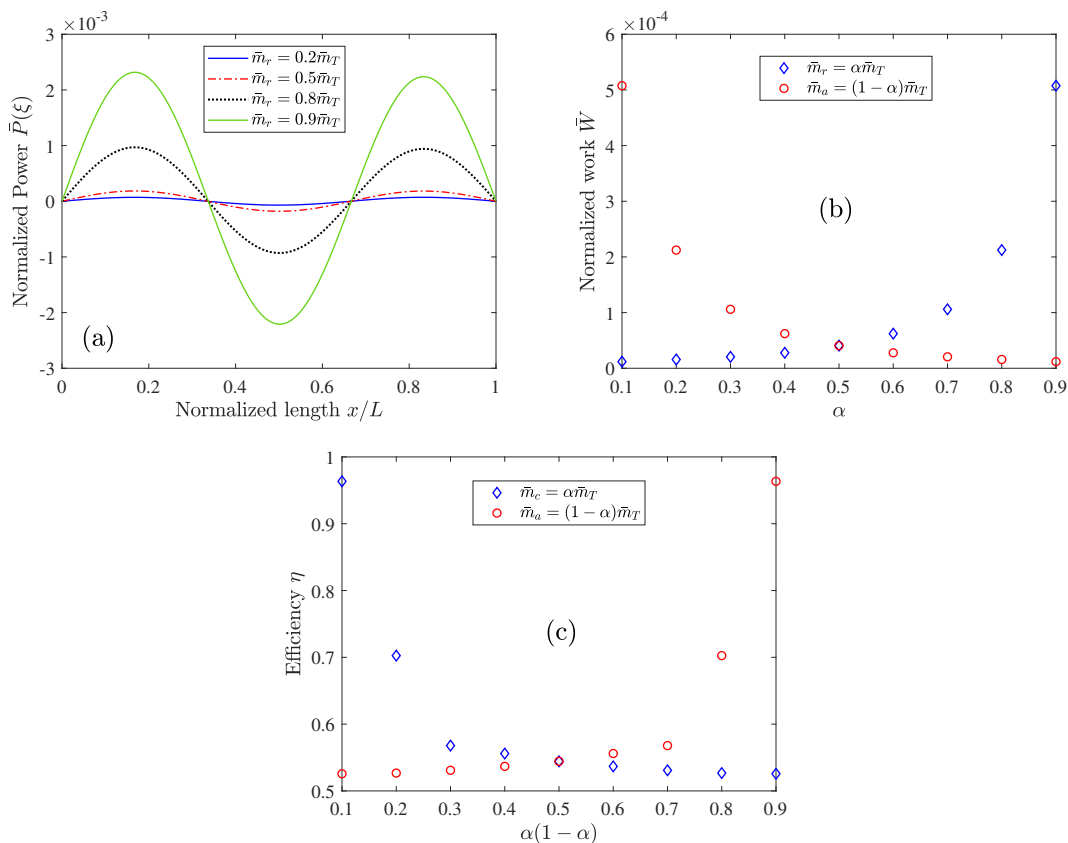


Figure 3.14: Effect of varying the relative mass ratio of the MDR. The analysis considers (a) the normalized power output, (b) the normalized work done on the cable, and (c) the dampers efficiency.

also significantly decrease to nearly half when the in-span mass is relatively larger than the suspended mass. We can conclude that for optimal performance of the MDR, it is necessary to minimize the in-span mass.

3.2.4 Two mobile damping robots

In this subsection, we study the effect of having two robots at each end of the conductor. Indeed, in the field, power line span can be on average as long as 200 meters. In these cases, having a single damper is not sufficient for vibration control. Therefore, we compare the performance in terms of vibration control for a single MDR and two MDR installed on a

conductor. Figure 3.15 shows the normalized power generated by the cable when subject to an input frequency matching ω_3 . From the Figure, we can see that adding the second MDR ensure that the vibration control is superior to that of a single MDR. However, from the figure, we can only estimate that the performance of having a single MDR is similar to that of having two MDR. However, when we compute the amount of work done on the cable for each case, the cable with two MDR decreases the work done on the cable by nearly half. Let \bar{W}_b be the work done on the cable with two MDR and \bar{W}_m , the work done on the cable with a single MDR. The numerical simulations show that $\bar{W}_b = 2.67 * 10^{-5}$ while $\bar{W}_m = 5.47 * 10^{-5}$. This observation suggest that if the MDR is an economically viable solution, having two robots on single line will improve vibration mitigation of power lines.

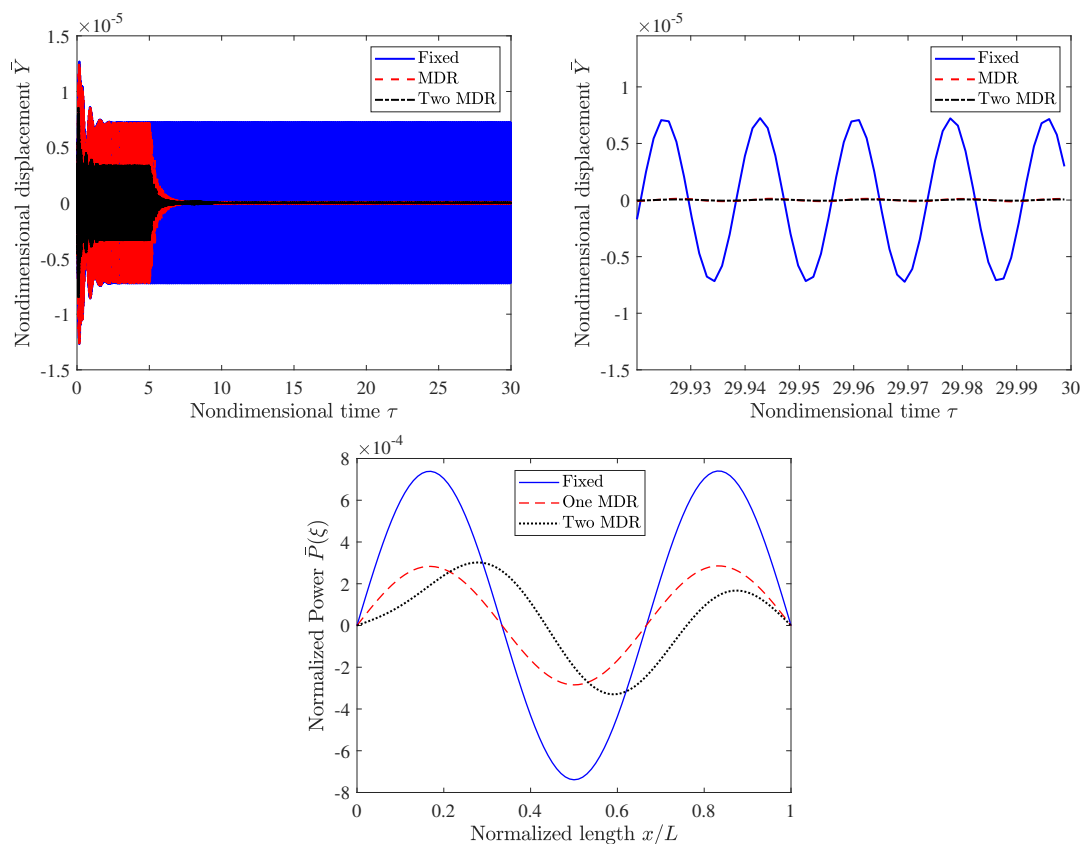


Figure 3.15: Comparing the normalized power on the cable for the fixed damper, a single MDR and two MDR as a function of normalized length.

3.2.5 Energy requirement of the mobile damping robot

The mobile damping robot presents a clear advantage to the fixed damper. However, to operate the controller, it is necessary to have an energy module that provide enough voltage to move the robot to the target antinode. We can determine this energy requirement by evaluating the total force requirement of the controller defined in Eq. 2.19. Figure 3.16 shows the normalized energy output from the controller as a function of the normalized frequency. The results show that as the selected input frequency increase, the energy requirement first decrease up to ω_{11} . This observation is expected as the number of antinode increase on the line. This reduces the distance to the antinode from the initial position of the robot. At ω_{11} , the initial position of the robot coincide with the antinode which reduces the energy requirement. Then as we continue to increase the input frequency, the initial position of the robot starts increase relative to the antinode. Overall, the energy requirement is substantial and finding a source of energy to move the robot is essential. In the subsequent analysis, we consider the possibility for energy harvesting to help cover some of the travel cost in terms of energy requirement to target antinodes.

3.3 Energy harvesting mobile damper performance

In the previous section, the numerical examples indicated that the mobile robot has a superior performance for vibration reduction when compared to the fixed damper, especially when the fixed damper coincide with a node. However, we have seen that the robot relies on an energy input to move to the antinode. It is therefore necessary to modify our design to include an energy harvesting device. In the mathematical modeling section 2.1, we introduced the electromagnetic shunt damper. This device is known to act as a damper while harvesting energy.

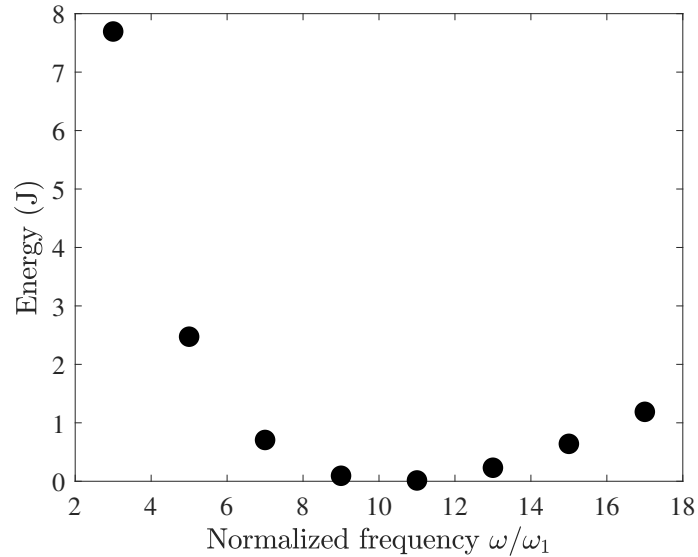


Figure 3.16: Assessing the energy requirement of the MDR as a function of the normalized input frequency.

In this section, we present the results of the energy harvesting mobile damping robot (EHMDR). We first compare the performance of the energy harvesting mobile robot to the mobile damping robot. Then we assess the advantages and disadvantages of the energy harvester. Finally, we perform a parametric study of the energy harvesting device.

3.3.1 Comparing the EHMDR to the MDR

Table 3.2 shows the parameters of the electromagnetic shunt mobile damping robot. The physical parameters are identical to those presented for the MDR. To obtain the shunted RLC circuit parameters, we needed to select practical values for that would have a reasonable size for a 5-kg mobile damping robot. The RLC parameters can be further tuned with the other parameters of the system to optimize both vibration control and energy harvesting. However, optimization of the parameters is not a focus of this study.

We begin the analysis of the EHMDR by comparing its performance to the mobile damping

Table 3.2: Parameters of the EHMDR

$m_r(\text{m})$	$m_a(\text{kg/m})$	$k(\text{N/m})$	k_f	$R(\Omega)$	$C(\mu\text{F})$	$L(\text{mH})$
0.2	4.8	$m_a * \omega_n^2$	12.6	1.3	10	41.8

robot and the conventional fixed damper. Figures 3.17-(a)-(d) show the normalized power of the cable as a function of normalized length. We observe that the energy harvesting mobile device significantly outperforms the fixed absorber and the MDR for all frequencies considered.

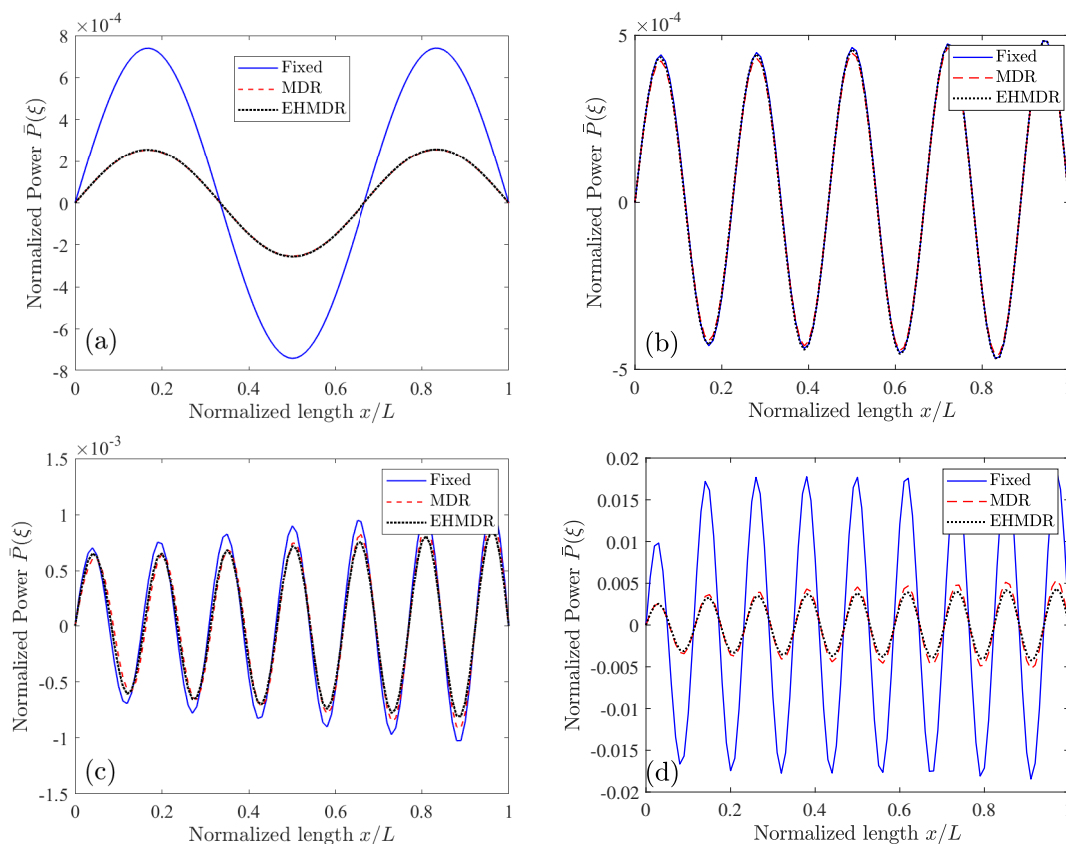


Figure 3.17: A comparison of the vibration control performance of the fixed damper, the MDR and the EHMDR for (a) ω_3 , (b) ω_9 , (c) ω_{13} and (d) ω_{17} .

As we have done in the aforementioned analysis, we can observe the performance of the dampers by studying the time response of the cable as well as the behaviors of its modes.

Figure 3.18-(a) shows the cable time function maximum amplitude when the excitation frequency matches the fundamental frequency. We can see that all the dampers are able to considerably reduce the time function magnitude of the first mode. Figure 3.18-(b) shows the time response of the cable for each damper. Similar to the MDR, the EHMDR is superior to the fixed damper. At transient state, the EHMDR has superior displacement than the other dampers. At steady state, the performance of the EHMDR is similar to the MDR performance (Fig. 3.18-(c)).

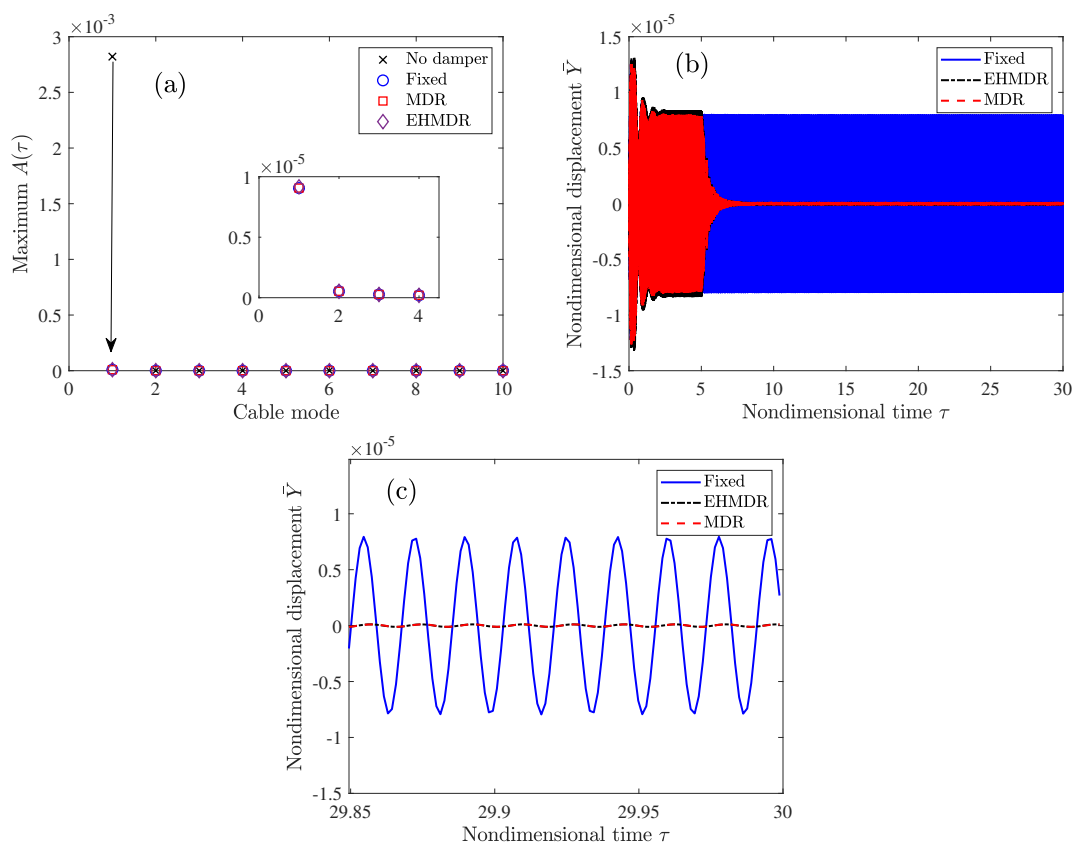


Figure 3.18: Time functions and time response of the cable comparing the performance of the EHMDR to the other dampers for ω_1 (Fig. 3.18 (a)-(c)).

We can also evaluate the amount of work done to the cable as well as the efficiency of each damper to have a holistic measure of the dampers performance. Figure 3.19-(a) shows that for all input frequencies, the EHMDR is able to maintain a similar cable vibration level

(less work done on the cable) than the MDR. This observation directly translate to similar efficiency in terms of vibration control for both the energy harvesting mobile device and the MDR. From these results, we understand that adding the electromagnetic transducer with the selected values of the RLC circuit does not degrade the performance of the EHMDR in terms of vibration control.

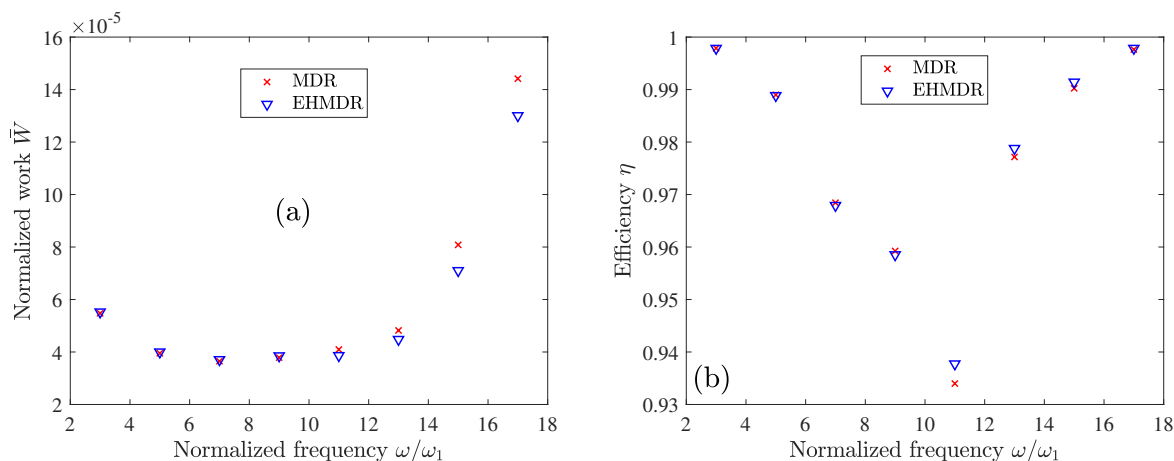


Figure 3.19: Assessing (a) the amount of work done on the cable and (b) the efficiency for the EHMDR when compared to the MDR.

We have established that the EHMDR outperforms the fixed and the MDR in terms of vibration mitigation. It is also necessary to determine if the energy harvested by the EHMDR is enough to cover the travel cost to the target antinode. Figure 3.20 shows energy as a function of the normalized frequency. The results suggest that the energy harvested by the EHMDR can not help cover the total energy requirement to move to target antinodes. We note that for energy values near ω_{13} , the EHMDR can cover near 10% of the energy requirement. However, overall, the EHMDR will need to be equipped with other sources of energy. Considering optimal values of the EHMDR may also help increasing the significance of energy harvesting. Additionally, the energy harvested can still serve other purposes such as power some of the electronics of the damping robot.

To have a better understanding of the energy transfer to the RLC circuit, we can study the

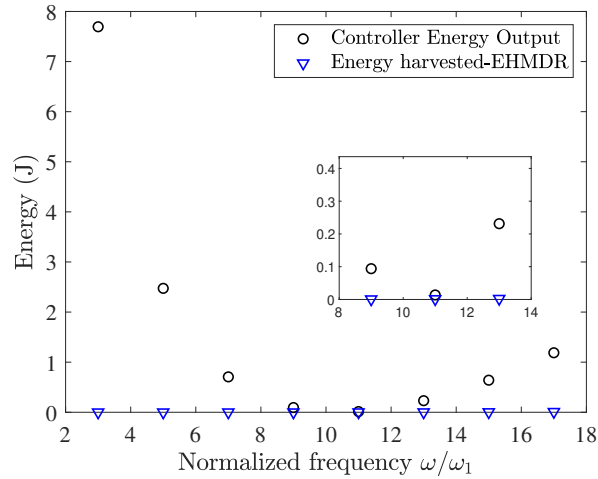


Figure 3.20: Comparing the energy output of the controller to the energy harvested by the EHMDR.

power variation for the EHMDR. Figure 3.21 shows the power harvested by the RLC circuit as a function of the nondimensional time when the cable is excited by the first (Fig.3.21-(a)) and the third mode (Fig. 3.21-(b)) respectively. It is important to note that the MDR is given a signal to move to the antinode after the first 5 normalized time. The results show that before the EHMDR moves, it harvest significantly more energy than when it starts moving to the antinode. This observation can be explain by the fact that initially, because the EHMDR is not at an antinode, there is a lot of energy available for energy harvesting. However, as the EHMDR moves, it reduces the vibration of the cable which directly affects the amount of energy harvested. From this analysis, we understand that the waiting period can be key to harvest enough energy to power some components of the EHMDR. As long as within the waiting period the vibration of the maximum displacement cable is within the acceptable limits, the potential for energy harvesting is promising.

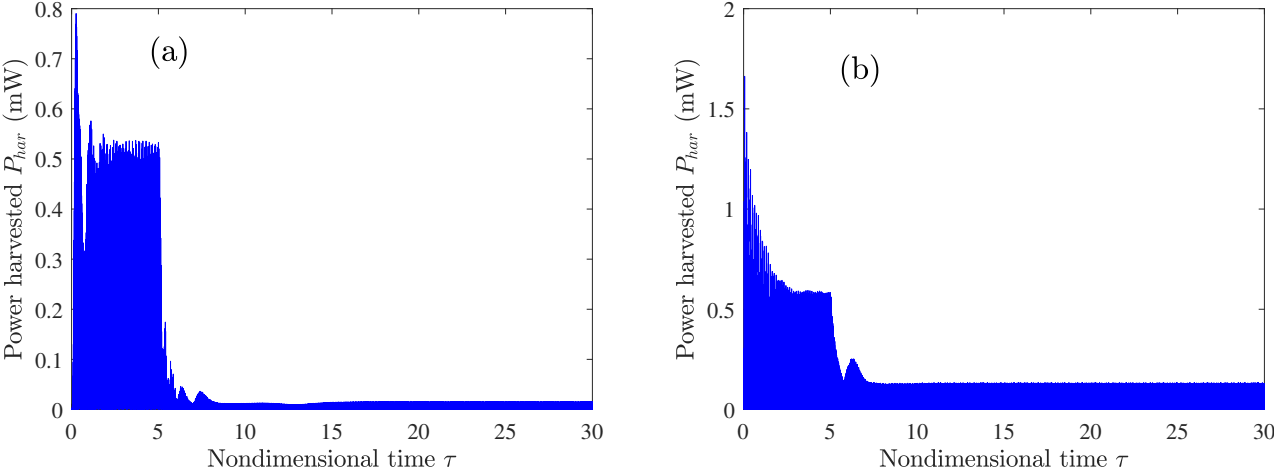


Figure 3.21: Determining the power harvested by the EHMDR when the cable is excited by the first and the third mode.

Chapter 4

Discussion

In this chapter, the results of the thesis are summarized. We have shown that the MDR presents multiple advantages when compared to the fixed damper. For the optimal location of the conventional fixed damper, the efficiency varies but can be substantial as long as the damper does not coincide with a vibration node. Using the MDR we can always ensure that we can move away from nodal points across the cable. Additionally, because the MDR move towards the points of maximum vibration, i.e., antinodes, the vibration mitigation is optimal. The study also focus on determining the appropriate k_p and k_d values for optimal control. Using the Linear-Quadratic Regulator built-in function in MATLAB, we demonstrated that to minimize percent overshoot as well as steady state error, k_d needs to be larger than k_p . This solution also ensures low input control value for energy requirement consideration.

Further parametric study showed that for optimal vibration control, the in-span mass needs to be minimized in favor of the suspended damper. The analysis clearly shows that having a larger in-span significantly decreases how much energy can be taken out of the conductor. Additional numerical analysis also focused on examining the performance of two robots attached at each end of the conductor. This analysis was conducted because on the field, conductor can span over more than 200 meters. To effectively control the vibrations, fixed dampers are installed at each end of the conductor. In this effort, we evaluated the performance of two MDR on a single conductor. The analysis shows that having two MDR decreases the amount of work done on the cable by nearly half.

The MDR initially presented had no energy module. However, because the PD controller has an energy requirement, we determined that the device needs enough voltage to move to the target antinode. As the frequency increases, the target antinode is closer to the initial location of the MDR. Nonetheless, the mobile device needs a power source to move. To meet this need, we studied the impact of adding an electromagnetic shunt damper to the MDR making it an EHMDR. We observed that the EHMDR has similar performance characteristics with the MDR with the appropriate choice of parameters.

Furthermore, we also studied the possibility of energy harvesting with the electromagnetic device. We selected practical RLC parameters. For the selected parameters, we observed that the energy harvested cannot help cover most of the cost of the harvest enough energy to cover the travel cost to the target antinode. Additional energy harvesting components such as solar will therefore need to be considered to achieved an self-powered mobile damping robot. Although energy harvesting in practice may not be fully achievable, the EHMDR can be consider as a start of a holistic solution to reduce vibration mitigation of the power lines based on the numerical analysis. The limited harvested energy can be used to power sensors and actuators embedded in the robot for power line monitoring and inspection. Additional study will need to be conducted to optimize the RLC parameters to maximize energy harvesting for the range of frequency required.

Chapter 5

Conclusions and Future work

5.1 Conclusions

In this thesis, a mobile damping robot (MDR) is proposed for wind-induced vibration (WIV) control of power lines. The proposed MDR is modeled and analyzed using Hamilton's principle and Galerkin decomposition method to determine its performance in terms of vibration mitigation of power lines. This work contributes to the ongoing research for continuous systems vibration mitigation. The proposed solution tracks the cable antinodes using a PD controller as the wind characteristic changes. The findings showed that for optimal control k_d needs to be larger than k_p . Considering the work done on the cable and the efficiency of the dampers, the mobile damping robot outperforms the fixed damper for all frequencies considered. When the fixed damper coincides with a node, the vibration levels are worse than the vibration of the cable with no damper as the cable goes to resonance. In this scenario, the mobility of the MDR becomes a significant advantage in limiting structural damages. The numerical examples also show that some of the energy dissipated by the MDR can be used to power the robot to the target antinode. In this effort, the proposed MDR is re-designed as a energy harvesting mobile damping robot (EHMDR) with an electromagnetic shunt damper. The results show that the EHMDR has similar performance with the MDR in terms of vibration reduction. Although, the study shows that for the selected parameters, the EHMDR cannot be self-powered through energy harvesting, some of the energy harvested can be used

for other small electronic components.

5.2 Future Work

The results obtained in this study show theoretically that the proposed MDR offers a significant advantage to the fixed damper. For future work, the following tasks need to be completed:

1. Nonlinear consideration need to be evaluated for the fixed damper and the MDR. Indeed, Stockbridge dampers are known to have highly nonlinear behavior. The impact of nonlinearity on the performance of the MDR needs to be assessed.
2. The numerical results need to be verified experimentally. To achieve this task, a prototype of the MDR needs to be realized. The mechanical design can be divided into five categories which are locomotion, clamping, mounting, communication and damping.
 - 2.1. The locomotion component will rely on a control scheme that can help determine changes in the vibration of the cable to readjust the position of the robot to the antinode. The locomotion is also directly directed to energy supply. The potential for energy harvesting will need to be realized and tested.
 - 2.2. For the clamping component, the design needs to be robust enough that the MDR can stay at a desired position when no input is given by the controller. That will ensure the stability of the robot on the cable for safety and life expectancy consideration.
 - 2.3. The mounting component of the MDR refers to an installment protocol that will be cost effective. For mounting and clamping, the design will rely on advances in inspection robots technology.

2.4. Having the MDR on the line, offers the possibility for online structural health monitoring (SMH). To help with SMH, the MDR needs to be designed with image acquisition devices. The data that is recorded on the line needs to be communicated to the ground. For this reason, adding a communication network scheme will be key to the success of the MDR. Different communication techniques including Bluetooth would need to be tested.

2.5. The damping component of the MDR is realized by using the 6R Asymmetric damper recently patented by Barry *et. al*, [15]. The damper will need to be securely attached to the locomotion component of the device. The resonant frequencies of the damper will need to be determined and tested for the experimental cable.

3. The control scheme developed in this study relies on a Proportional-Derivative controller. In practice using other control techniques maybe more robust and cost effective. One key consideration is to design a trajectory planning scheme for the controller. Indeed, determining the maximum displacement of the cable is difficult task. For the resonant case, we can proceed using wind sensors and similar devices. However, we will need to consider the non-uniform, random wind excitation case in future work. Defining an appropriate cost function and building a trajectory will be a major challenge for future research and for a successful product. The control scheme will need to be experimentally tested for accuracy and robust.

The successful completion of the aforementioned tasks will lead to the development of a fully functional prototype that will be used as a base for the deployment of the MDR in the field for power line protection and monitoring.

Bibliography

- [1] Ozgur B Akan, Oktay Cetinkaya, Caglar Koca, and Mustafa Ozger. Internet of hybrid energy harvesting things. *IEEE Internet of Things Journal*, 5(2):736–746, 2017.
- [2] Ahmad Bala Alhassan, Xiaodong Zhang, Haiming Shen, and Haibo Xu. Power transmission line inspection robots: A review, trends and challenges for future research. *International Journal of Electrical Power & Energy Systems*, 118:105862, 2020.
- [3] Randa Almadhoun, Tarek Taha, Lakmal Seneviratne, Jorge Dias, and Guowei Cai. A survey on inspecting structures using robotic systems. *International Journal of Advanced Robotic Systems*, 13(6):1729881416663664, 2016.
- [4] Gustavo RS Assi. Wake-induced vibration of tandem and staggered cylinders with two degrees of freedom. *Journal of Fluids and Structures*, 50:340–357, 2014.
- [5] Baruch Avidar. Electronic airborne inspection method for overhead transmission powerlines. In *Proceedings of ESMO'93. IEEE 6th International Conference on Transmission and Distribution Construction and Live-Line Maintenance*, pages 89–93. IEEE, 1993.
- [6] VI Babitsky and AM Vepruk. Damping of beam forced vibration by a moving washer. *Journal of Sound and Vibration*, 166(1):77–85, 1993.
- [7] MA Baenziger, WD James, Brent Wouters, and Li Li. Dynamic loads on transmission line structures due to galloping conductors. *IEEE Transactions on Power Delivery*, 9(1):40–49, 1994.
- [8] O Barry, JW Zu, and DCD Oguamanam. Analytical and experimental investigation of

- overhead transmission line vibration. *Journal of Vibration and Control*, 21(14):2825–2837, 2015.
- [9] O Barry, R Long, and DCD Oguamanam. Rational damping arrangement design for transmission lines vibrations: analytical and experimental analysis. *Journal of Dynamic Systems, Measurement, and Control*, 139(5), 2017.
- [10] O Barry, R Long, and DCD Oguamanam. Simplified vibration model and analysis of a single-conductor transmission line with dampers. *Proceedings of the Institution of Mechanical Engineers, Part C: Journal of Mechanical Engineering Science*, 231(22):4150–4162, 2017.
- [11] Oumar Barry and Mohammad Bukhari. On the modeling and analysis of an energy harvester moving vibration absorber for power lines. In *ASME 2017 Dynamic Systems and Control Conference*. American Society of Mechanical Engineers Digital Collection, 2017.
- [12] Oumar Barry, Donatus CD Oguamanam, and Der Chyan Lin. Aeolian vibration of a single conductor with a stockbridge damper. *Proceedings of the Institution of Mechanical Engineers, Part C: Journal of Mechanical Engineering Science*, 227(5):935–945, 2013.
- [13] Oumar Barry, Jean Zu, and DCD Oguamanam. Vibration analysis of stockbridge dampers: Experimental verification. *Proceedings of the 24th CANCAM Saskatoon, Saskatchewan, Canada*, 2013.
- [14] Oumar Barry, JW Zu, and DCD Oguamanam. Nonlinear dynamics of stockbridge dampers. *Journal of Dynamic Systems, Measurement, and Control*, 137(6):061017, 2015.

- [15] Oumar Rafiou Barry, Emadeddin Y Tanbour, Nitish Kumar Vaja, and Hesham Tanbour. Asymmetric aeolian vibration damper, April 17 2018. US Patent 9,948,081.
- [16] Rafiou Oumar Barry. *Vibration Modeling and Analysis of a Single Conductor With Stockbridge Dampers*. PhD thesis, University of Toronto, 2014.
- [17] S P Beeby, M J Tudor, and NM White. Energy harvesting vibration sources for microsystems applications. *Measurement science and technology*, 17(12):R175, 2006.
- [18] Sam Behrens, Andrew J Fleming, and SO Reza Moheimani. Passive vibration control via electromagnetic shunt damping. *IEEE/ASME transactions on mechatronics*, 10(1):118–122, 2005.
- [19] M Bukhari, A Malla, H Kim, O Barry, and L Zuo. On a self-tuning sliding-mass electromagnetic energy harvester. *AIP Advances*, 10(9):095227, 2020.
- [20] NB Caldwell and MF Daqaq. Exploiting the principle parametric resonance of an electric oscillator for vibratory energy harvesting. *Applied Physics Letters*, 110(9):093903, 2017.
- [21] Ian L Cassidy, Jeffrey T Scruggs, Sam Behrens, and Henri P Gavin. Design and experimental characterization of an electromagnetic transducer for large-scale vibratory energy harvesting applications. *Journal of Intelligent Material Systems and Structures*, 22(17):2009–2024, 2011.
- [22] John Chan, Dave Havard, Chuck Rawlins, Giorgio Diana, Louis Cloutier, Jean-Louis Lilien, Claude Hardy, Jeff Wang, and Anand Goel. Epr transmission line reference book: wind-induced conductor motion. 2009.
- [23] Wenkai Chang, Guodong Yang, Junzhi Yu, Zize Liang, Long Cheng, and Chao Zhou. Development of a power line inspection robot with hybrid operation modes. In *2017*

- IEEE/RSJ International Conference on Intelligent Robots and Systems (IROS)*, pages 973–978. IEEE, 2017.
- [24] Tai-Hong Cheng and Il-Kwon Oh. A current-flowing electromagnetic shunt damper for multi-mode vibration control of cantilever beams. *Smart Materials and Structures*, 18(9):095036, 2009.
- [25] Kyeong Ho Cho, Young Hoon Jin, Ho Moon Kim, Hyungpil Moon, Ja Choon Koo, and Hyouk Ryeol Choi. Multifunctional robotic crawler for inspection of suspension bridge hanger cables: Mechanism design and performance validation. *IEEE/ASME Transactions on Mechatronics*, 22(1):236–246, 2016.
- [26] YM Desai, P Yu, N Popplewell, and AH Shah. Finite element modelling of transmission line galloping. *Computers & structures*, 57(3):407–420, 1995.
- [27] US EPRI and EDF R&D. Profiling and mapping of intelligent grid r&d programs. Technical report, Palo Alto, CA: US EPRI, 2006.
- [28] Alper Erturk and Daniel J Inman. *Piezoelectric energy harvesting*. John Wiley & Sons, 2011.
- [29] Kangqi Fan, Qinxue Tan, Yiwei Zhang, Shaohua Liu, Meiling Cai, and Yingmin Zhu. A monostable piezoelectric energy harvester for broadband low-level excitations. *Applied Physics Letters*, 112(12):123901, 2018.
- [30] Jixiong Fei, Bin Lin, Shuai Yan, Mei Ding, Juliang Xiao, Jin Zhang, Xiaofeng Zhang, Chunhui Ji, and Tianyi Sui. Chatter mitigation using moving damper. *Journal of Sound and Vibration*, 410:49–63, 2017.
- [31] AJ Fleming, S Behrens, and SOR Moheimani. Reducing the inductance requirements of piezoelectric shunt damping systems. *Smart materials and structures*, 12(1):57, 2003.

- [32] Robert L Forward. Electronic damping of vibrations in optical structures. *Applied optics*, 18(5):690–697, 1979.
- [33] Hermann Frahm. Device for damping vibrations of bodies., April 18 1911. US Patent 989,958.
- [34] Brendan Gates. A power line inspector device. 2013.
- [35] P Hagedorn. Wind-excited vibrations of transmission lines: A comparison of different mathematical models. *Mathematical Modelling*, 8:352–358, 1987.
- [36] Nesbitt W Hagood and Andreas von Flotow. Damping of structural vibrations with piezoelectric materials and passive electrical networks. *Journal of sound and vibration*, 146(2):243–268, 1991.
- [37] Malcolm John Hudson and Paul Reynolds. Implementation considerations for active vibration control in the design of floor structures. *Engineering Structures*, 44:334–358, 2012.
- [38] Ji Hoon Hyun, Long Huang, and Dong Sam Ha. Vibration and thermal energy harvesting system for automobiles with impedance matching and wake-up. In *2018 IEEE international symposium on circuits and systems (ISCAS)*, pages 1–5. IEEE, 2018.
- [39] Daniel J Inman and Ramesh Chandra Singh. *Engineering vibration*, volume 3. Prentice Hall Englewood Cliffs, NJ, 1994.
- [40] M Jafari, F Hou, and A Abdelkefi. Wind-induced vibration of structural cables. *Non-linear Dynamics*, 100(1):351–421, 2020.
- [41] Nader Jalili. A comparative study and analysis of semi-active vibration-control systems. *Journal of vibration and acoustics*, 124(4):593–605, 2002.

- [42] Dewi Jones and Graham Earp. Requirements for aerial inspection of overhead electrical power lines. In *RPVs International Conference, 12 th, Bristol, United Kingdom*, 1996.
- [43] Jaka Katrasnik, Franjo Pernus, and Bostjan Likar. A survey of mobile robots for distribution power line inspection. *IEEE Transactions on power delivery*, 25(1):485–493, 2009.
- [44] Heung Soo Kim, Joo-Hyong Kim, and Jaehwan Kim. A review of piezoelectric energy harvesting based on vibration. *International journal of precision engineering and manufacturing*, 12(6):1129–1141, 2011.
- [45] Hongjip Kim, Arthur Smith, Oumar Barry, and Lei Zuo. Self-resonant energy harvester with a passively tuned sliding mass. In *ASME 2019 Dynamic Systems and Control Conference*. American Society of Mechanical Engineers Digital Collection, 2019.
- [46] Jeong-Hoi Koo, Mehdi Ahmadian, Mehdi Setareh, and Thomas Murray. In search of suitable control methods for semi-active tuned vibration absorbers. *Journal of Vibration and Control*, 10(2):163–174, 2004.
- [47] Matthew A Lackner and Mario A Rotea. Passive structural control of offshore wind turbines. *Wind energy*, 14(3):373–388, 2011.
- [48] Zhongjie Li, Lei Zuo, George Luhrs, Liangjun Lin, and Yi-xian Qin. Electromagnetic energy-harvesting shock absorbers: design, modeling, and road tests. *IEEE Transactions on vehicular technology*, 62(3):1065–1074, 2012.
- [49] GJ Liao, XL Gong, CJ Kang, and SH Xuan. The design of an active–adaptive tuned vibration absorber based on magnetorheological elastomer and its vibration attenuation performance. *Smart materials and structures*, 20(7):075015, 2011.

- [50] Jean-Louis Lilien and Dmitri Snegovski. Wake-induced vibration in power transmission line. parametric study. *Flow Induced Vibration-FIV 2004*, page 5, 2004.
- [51] Eduardo José Lima, Marcelo Henrique Souza Bomfim, and Miguel Augusto de Miranda Mourão. Polibot–power lines inspection robot. *Industrial Robot: An International Journal*, 2018.
- [52] ML Lu and JK Chan. An efficient algorithm for aeolian vibration of single conductor with multiple dampers. *IEEE Transactions on power Delivery*, 22(3):1822–1829, 2007.
- [53] Guo-ming Ma, Ya-bo Li, Nai-qiang Mao, Cheng Shi, Cheng-rong Li, and Bo Zhang. A fiber bragg grating-based dynamic tension detection system for overhead transmission line galloping. *Sensors*, 18(2):365, 2018.
- [54] Pukar Maharjan, Md Salauddin, Hyunok Cho, and Jae Yeong Park. An indoor power line based magnetic field energy harvester for self-powered wireless sensors in smart home applications. *Applied energy*, 232:398–408, 2018.
- [55] John McCombe. *Overhead line practice*. Macdonald, 1955.
- [56] MH Miguelez, L Rubio, JA Loya, and J Fernandez-Saez. Improvement of chatter stability in boring operations with passive vibration absorbers. *International Journal of Mechanical Sciences*, 52(10):1376–1384, 2010.
- [57] Lindsay M Miller, Pit Pillatsch, Einar Halvorsen, Paul K Wright, Eric M Yeatman, and Andrew S Holmes. Experimental passive self-tuning behavior of a beam resonator with sliding proof mass. *Journal of Sound and Vibration*, 332(26):7142–7152, 2013.
- [58] Rebecca Miller, Farshid Abbasi, and Javad Mohammadpour. Power line robotic device for overhead line inspection and maintenance. *Industrial Robot: An International Journal*, 2017.

- [59] Rohit Moghe, Amrit R Iyer, Frank C Lambert, and Deepak Divan. A low-cost electric field energy harvester for an mv/hv asset-monitoring smart sensor. *IEEE Transactions on Industry Applications*, 51(2):1828–1836, 2014.
- [60] SO Reza Moheimani. A survey of recent innovations in vibration damping and control using shunted piezoelectric transducers. *IEEE transactions on control systems technology*, 11(4):482–494, 2003.
- [61] H Moradi, F Bakhtiari-Nejad, and MR Movahhedy. Tuneable vibration absorber design to suppress vibrations: an application in boring manufacturing process. *Journal of Sound and Vibration*, 318(1-2):93–108, 2008.
- [62] Rosario Morello, Subhas C Mukhopadhyay, Zheng Liu, Daniel Slomovitz, and Subhansu Ranjan Samantaray. Advances on sensing technologies for smart cities and power grids: A review. *IEEE Sensors Journal*, 17(23):7596–7610, 2017.
- [63] Hyun Myung, Yang Wang, SC Kang, and XiaoQi Chen. Survey on robotics and automation technologies for civil infrastructure. 2014.
- [64] President’s Council of Economic Advisers. Economic benefits of increasing electric grid resilience to weather outages. 1:163–178, 2013.
- [65] CBSInternational Journal of Mechanical Sciences. 4,000 dte customers remain without power nearly a week after damaging winds. 1:163–178, 2017.
- [66] Mustafa Ozger, Oktay Cetinkaya, and Ozgur B Akan. Energy harvesting cognitive radio networking for iot-enabled smart grid. *Mobile Networks and Applications*, 23(4): 956–966, 2018.
- [67] Andrew Phillips, Eric Engdahl, Drew McGuire, Mark Major, and Glynn Bartlett. Autonomous overhead transmission line inspection robot (ti) development and demonstra-

- tion. In *2012 2nd International Conference on Applied Robotics for the Power Industry (CARPI)*, pages 94–95. IEEE, 2012.
- [68] Nicolas Pouliot, Pierre-Luc Richard, and Serge Montambault. Linescout technology opens the way to robotic inspection and maintenance of high-voltage power lines. *IEEE Power and Energy Technology Systems Journal*, 2(1):1–11, 2015.
- [69] A Rezaei and MH Sadeghi. Analysis of aeolian vibrations of transmission line conductors and extraction of damper optimal placement with a comprehensive methodology. *International Journal of Engineering*, 31(9):328–337, 2019.
- [70] Navid Asmari Saadabad, Hamed Moradi, and Gholamreza Vossoughi. Semi-active control of forced oscillations in power transmission lines via optimum tuneable vibration absorbers: with review on linear dynamic aspects. *International Journal of Mechanical Sciences*, 87:163–178, 2014.
- [71] Farhad S Samani and Francesco Pellicano. Vibration reduction on beams subjected to moving loads using linear and nonlinear dynamic absorbers. *Journal of Sound and Vibration*, 325(4-5):742–754, 2009.
- [72] Ibrahim Sari, Tuna Balkan, and Haluk Kulah. An electromagnetic micro power generator for wideband environmental vibrations. *Sensors and Actuators A: Physical*, 145:405–413, 2008.
- [73] Gennaro Scarselli, Francesco Nicassio, Fulvio Pinto, Francesco Ciampa, Onorio Iervolino, and Michele Meo. A novel bistable energy harvesting concept. *Smart Materials and Structures*, 25(5):055001, 2016.
- [74] Wenai Shen, Songye Zhu, Hongping Zhu, You Lin Xu, et al. Electromagnetic energy

- harvesting from structural vibrations during earthquakes. *Smart Struct. Syst*, 18(3):449–470, 2016.
- [75] Rohit Somkuwar, Jaya Chandwani, and Raghavendra Deshmukh. Wideband auto-tunable vibration energy harvester using change in centre of gravity. *Microsystem Technologies*, 24(7):3033–3044, 2018.
- [76] G Stockbridge. Vibration damper patent no. 1675391. *USA patent Office*, 1925.
- [77] Sujesha Sudevalayam and Purushottam Kulkarni. Energy harvesting sensor nodes: Survey and implications. *IEEE Communications Surveys & Tutorials*, 13(3):443–461, 2010.
- [78] JQ Sun, M Re Jolly, and MA Norris. Passive, adaptive and active tuned vibration absorbers—a survey. *Journal of Vibration and Acoustics*, 117(B):234–242, 1995.
- [79] Xiudong Tang, Teng Lin, and Lei Zuo. Design and optimization of a tubular linear electromagnetic vibration energy harvester. *IEEE/ASME Transactions on Mechatronics*, 19(2):615–622, 2013.
- [80] Sanjiv G Tewani, Keith E Rouch, and Bruce L Walcott. A study of cutting process stability of a boring bar with active dynamic absorber. *International Journal of Machine Tools and Manufacture*, 35(1):91–108, 1995.
- [81] NK Vaja, OR Barry, and EY Tanbour. On the modeling and analysis of a vibration absorber for overhead powerlines with multiple resonant frequencies. *Engineering Structures*, 175:711–720, 2018.
- [82] J Vecchiarelli, IG Currie, and DG Havard. Computational analysis of aeolian conductor vibration with a stockbridge-type damper. *Journal of Fluids and Structures*, 14(4):489–509, 2000.

- [83] Jack Vecchiarelli. *Aeolian vibration of a conductor with a Stockbridge-type damper*. PhD thesis, 1998.
- [84] Pankaj Wahi and Anindya Chatterjee. Self-interrupted regenerative metal cutting in turning. *International Journal of Non-Linear Mechanics*, 43(2):111–123, 2008.
- [85] Dung-An Wang, Chun-Yuan Chiu, and Huy-Tuan Pham. Electromagnetic energy harvesting from vibrations induced by kármán vortex street. *Mechatronics*, 22(6):746–756, 2012.
- [86] YR Wang and CY Lo. Design of hybrid dynamic balancer and vibration absorber. *Shock and Vibration*, 2014, 2014.
- [87] Bo Yan, Hongye Ma, Ning Yu, Lu Zhang, and Chuanyu Wu. Theoretical modeling and experimental analysis of nonlinear electromagnetic shunt damping. *Journal of Sound and Vibration*, 471:115184, 2020.
- [88] Liman Yang, Chenyao Fu, Yunhua Li, and Lianming Su. Survey and study on intelligent monitoring and health management for large civil structure. *International Journal of Intelligent Robotics and Applications*, 3(3):239–254, 2019.
- [89] Ufuk Yigit, Ender Cigeroglu, and Erhan Budak. Chatter reduction in boring process by using piezoelectric shunt damping with experimental verification. *Mechanical Systems and Signal Processing*, 94:312–321, 2017.
- [90] Ming Yuan, Ziping Cao, Jun Luo, and Xiujian Chou. Recent developments of acoustic energy harvesting: A review. *Micromachines*, 10(1):48, 2019.
- [91] Masoud Zarepoor and Onur Bilgen. Constrained-energy cross-well actuation of bistable structures. *AIAA journal*, 54(9):2905–2908, 2016.

- [92] Wanlu Zhou, Gopinath Reddy Penamalli, and Lei Zuo. An efficient vibration energy harvester with a multi-mode dynamic magnifier. *Smart Materials and Structures*, 21(1):015014, 2011.
- [93] Lei Zuo and Wen Cui. Dual-functional energy-harvesting and vibration control: electromagnetic resonant shunt series tuned mass dampers. *Journal of vibration and acoustics*, 135(5), 2013.
- [94] Lei Zuo and Xiudong Tang. Large-scale vibration energy harvesting. *Journal of intelligent material systems and structures*, 24(11):1405–1430, 2013.

Appendices

Appendix A

Matlab code

```
1 %code written by: Paul-Camille Kakou
2
3 %this code generates the dynamics of the mobile damping robot ,
4 %energy harvester mobile damping robot and fixed damper
5 %on a simple supported beam (conductor)
6
7 tic %Start watch
8 format
9 clear;clc; close all;
10 %=====
11 % Initialization
12 %=====
13 %Parameters of the cable
14 n=5;
15 mode=3;
16 m=1.6286;%beam mass per length
17 Te=27840;%Tension
18 L=27.25;% Length
19 EI=1602;% Flexural rigidity
20
21 %=====
22 % Computation
23 %=====
24 for i=1:5
```

```

25 Run_mode=i;
26 count=Run_mode;
27 switch Run_mode
28
29 case 1 %Fixed damper mode
30
31 [PB,PE,PR,PF,PM,loc]=nondim(Run_mode,n,Te,L,m,EI,mode);
32 [x0,tSpan]=iconds(Run_mode,PM,n,mode,loc);
33
34 % this solves the system
35 [tau,x]=ode45(@(tt,xx) modelfun(tt,xx,PB,PR,PE,PF,PM,count,mode,loc),
36 tSpan,x0);
37
38 %Time response of cable
39 q1_fixed=x(:,1:(end/2-3)); q1dt_fixed=x(:,(end/2+1):(end-3));
40
41 %Time response of damper
42 q2_fixed=x(:,(end/2-2):end/2-1); q2dt_fixed=x(:,(end-2):end-1);
43
44 %Time response of circuit
45 q3_fixed=x(:,(end/2)); q3dt_fixed=x(:,end);
46
47 case 2 %Moving damper
48 [PB,PE,PR,PF,PM,loc]=nondim(Run_mode,n,Te,L,m,EI,mode);
49 [x0,tSpan]=iconds(Run_mode,PM,n,mode,loc);
50
51 % this solves the system
52 [tau,x]=ode45(@(tt,xx) modelfun(tt,xx,PB,PR,PE,PF,PM,count,mode,loc),
53 tSpan,x0);

```

```

54 %Time response of cable
55 q1_mdr=x(:,1:(end/2-3));
56 q1dt_mdr=x(:,(end/2+1):(end-3));
57
58 %Time response of damper
59
60 q2_mdr=x(:,(end/2-2):end/2-1);
61 q2dt_mdr=x(:,(end-2):end-1);
62
63 %Time response of circuit
64 q3_mdr=x(:,(end/2));
65 q3dt_mdr=x(:,end);
66 case 3 %Mobile damper with energy harvester
67 [PB,PE,PR,PF,PM,loc]=nondim(Run_mode,n,Te,L,m,EI,mode);
68 [x0,tSpan]=iconds(Run_mode,PM,n,mode,loc);
69
70 % this solves the system
71 [tau,x]=ode45(@(tt,xx) modelfun(tt,xx,PB,PR,PE,PF,PM,count,mode,loc),
72             tSpan,x0);
73
74 %Time response of cable
75 q1_ehmdr=x(:,1:(end/2-3));
76 q1dt_ehmdr=x(:,(end/2+1):(end-3));
77
78 %Time response of damper
79
80 q2_ehmdr=x(:,(end/2-2):end/2-1);
81 q2dt_ehmdr=x(:,(end-2):end-1);
82
83 %Time response of circuit
84 q3_ehmdr=x(:,(end/2));

```

```

84     q3dt_ehmdr=x(:,end);
85 case 4 %No damper mode
86     [PB,PE,PR,PF,PM,loc]=nondim(Run_mode,n,Te,L,m,EI,mode);
87     [x0,tSpan]=iconds(Run_mode,PM,n,mode,loc);
88
89     % this solves the system
90     [tau,x]=ode45(@(tt,xx) modelfun(tt,xx,PB,PR,PE,PF,PM,count,mode,loc),
91                 tSpan,x0);
92
93     %Time response of cable
94     q1_o=x(:,1:(end/2-3));
95     q1dt_o=x(:,(end/2+1):(end-3));
96
97     %Time response of damper
98     q2_o=x(:,(end/2-2):end/2-1);
99     q2dt_o=x(:,(end-2):end-1);
100
101     %Time response of circuit
102     q3_o=x(:,(end/2));
103     q3dt_o=x(:,end);
104
105 case 5 %Two mobile damper mode
106     [PB,PR,PF,PM,loc]=nondim2(Run_mode,n,Te,L,m,EI,mode);
107     [x0,tSpan]=iconds(Run_mode,PM,n,mode,loc);
108
109     % this solves the system
110     [tau,x]=ode45(@(tt,xx) modelfun2(tt,xx,PB,PR,PF,PM,count,mode,loc),
111                 tSpan,x0);
112
113     %Time response of cable

```

```

113     q1_b=x(:,1:(end/2-4),1);
114     q1dt_b=x(:,(end/2+1):(end-4),1);
115
116     %Time response of left damper
117     q2_left=x(:,(end/2-3):end/2-2,1);
118     q2dt_left=x(:,(end-3):end-2,1);
119
120     %Time response of right damper
121     q3_right=x(:,(end/2-1):end/2,1);
122     q3dt_right=x(:,(end-1):end,1);
123 end
124 end
125
126 %=====
127 % Pst-processing & Results
128 %=====
129 close all
130
131 % Calculate the normalized power and work for each case
132 axialFrequency=PM(:,2);
133 amp_=PF(2);
134 w=PM(:,1);
135 xx=0:0.01:1;
136 moe_s=sqrt(2)*sin(axialFrequency(:)*xx);
137 G_f=amp_*sin(w(mode)*tau).*q1dt_fixed*moe_s;
138 G_m=amp_*sin(w(mode)*tau).*q1dt_mdr*moe_s;
139 G_e=amp_*sin(w(mode)*tau).*q1dt_ehmdr*moe_s;
140 G_o=amp_*sin(w(mode)*tau).*q1dt_o*moe_s;
141 G_b=amp_*sin(w(mode)*tau).*q1dt_b*moe_s;
142
143 Ib=trapz(tau,G_b); Im=trapz(tau,G_m); If=trapz(tau,G_f);

```

```

144 Ie=trapz(tau,G_e); Io=trapz(tau,G_o);
145
146 Wm=trapz(xx,Im); Wf=trapz(xx,If); We=trapz(xx,Ie);
147 Wo=trapz(xx,Io); Wb=trapz(xx,Ib);
148
149 %calculate the efficiency for each case
150 [n_f,n_m,n_e,n_b]=eff(Wo,Wf,Wm,We,Wb);
151
152 %Calculate the energy required to move the robot
153 p=pi/2/axialFrequency(mode);
154 Fc_mdr=zeros(n,1);
155 Fc_ehmdr=zeros(n,1);
156 kp_=PR(4);
157 kd_=PR(5);
158 step=1;
159
160 for kk=1:length(q2_mdr(:,1))
161     if round(p-q2_mdr(step,1),3)==0
162         break
163     end
164     Fc_mdr(step,:)=kp_*(p-q2_mdr(step,1))+kd_*(-q2dt_mdr(step,1));
165     step=step+1;
166 end
167 Ec_mdr=trapz(Fc_mdr.*q2dt_mdr(1:length(Fc_mdr),1));
168
169 % Plots
170 figure(1)
171 plot(xx,If,'b-', 'linewidth',1)
172 hold on
173 plot(xx,Im,'r-', 'linewidth',1)
174 plot(xx,Ib,'k:', 'linewidth',1.5)

```

```

175 xlabel('Normalized length  $x/L$ ','interpreter','latex')
176 ylabel('Normalized Power  $\bar{P}(x)$ ','interpreter','latex')
177 legend('Fixed','One MDR','Two MDR','interpreter','latex')
178 set(gca,'FontName','Times New Roman','FontSize',14)
179
180 l=0.5;%pi/2/axialFrequency(mode);
181 q0_f=sqrt(2)*q1_fixed*sin(PM(:,2)*l);
182 q0_m=sqrt(2)*q1_mdr*sin(PM(:,2)*l);
183 q0_e=sqrt(2)*q1_ehmdr*sin(PM(:,2)*l);
184 q0_o=sqrt(2)*q1_o*sin(PM(:,2)*l);
185 q0_b=sqrt(2)*q1_b*sin(PM(:,2)*l);
186
187 figure(2)
188 plot(tau,q0_f,'b')
189 hold on
190 plot(tau,q0_e,'r')
191 %plot(tau,q0_m,'k')
192 plot(tau,q0_b,'k')
193 xlabel('Nondimensional time  $\tau$ ','interpreter','latex')
194 ylabel('Nondimensional displacement  $\bar{Y}$ ','interpreter','latex')
195
196 %=====
197 % plotting animated vibration of cable for each case
198 %=====
199
200 q1=q1_b;
201
202 q2=q2_left;
203
204 q3=q3_right;
205

```

```

206 LSpan=linspace(0,1,101);
207 LWave=q1(:, :)*sqrt(2)*sin(axialFrequency(:)*LSpan); % Beam wave shape
208 RobotUpDownPosL=q1(1, :)*sqrt(2)*sin(axialFrequency(:)*q2(1,1)); % Robot
    position
209 RobotUpDownPosR=q1(1, :)*sqrt(2)*sin(axialFrequency(:)*q3(1,1)); % Robot
    position
210 figure(11)
211 wavePlot=plot(LSpan,(LWave(1, :)), 'b', 'lineWidth', 2);
212 axis([0 1 2*max(max(abs(LWave)))*[-1 1]]);
213 hold on
214 robotSpotL=plot(q2(1), RobotUpDownPosL, '*', 'Color', 'r', 'MarkerSize', 10);
215 robotSpotR=plot(q3(1), RobotUpDownPosR, '*', 'Color', 'k', 'MarkerSize', 10);
216 hold off
217
218 for ii=(numel(tSpan)-1)*0+1:500:numel(tSpan)
219
220     RobotUpDownPosL=q1(ii, :)*sqrt(2)*sin(axialFrequency(:)*q2(ii,1)); %
        Eigenfunction at Robot Position
221     RobotUpDownPosR=q1(ii, :)*sqrt(2)*sin(axialFrequency(:)*q3(ii,1)); %
        Eigenfunction at Robot Position
222     wavePlot.set('YData', LWave(ii, :));
223     robotSpotL.set('XData', q2(ii, 1), 'YData', RobotUpDownPosL);
224     robotSpotR.set('XData', q3(ii, 1), 'YData', RobotUpDownPosR);
225     drawnow;
226     xlabel('Normalized length', 'interpreter', 'latex')
227     ylabel('Normalized displacement', 'interpreter', 'latex')
228     set(gca, 'FontName', 'Times New Roman', 'FontSize', 14)
229     set(gcf, 'color', 'w'); % set figure background to white
230     drawnow;
231     frame = getframe;
232     im = frame2im(frame);

```

```

233     [imind ,cm] = rgb2ind(im,256);
234     outfile = 'twomotion.gif';
235
236     % On the first loop, create the file. In subsequent loops, append.
237     if ii==1
238         imwrite(imind ,cm, outfile , 'gif' , 'DelayTime' ,0 , 'loopcount' , inf);
239     else
240         imwrite(imind ,cm, outfile , 'gif' , 'DelayTime' ,0 , 'writemode' , 'append' );
241     end
242
243 end
244
245 close all
246 toc %stop watch
247 function [n_f,n_m,n_e,n_b]=eff(Wo,Wf,Wm,We,Wb)
248 if Wo>Wf
249     E_e=Wo-We;
250     E_mov=Wo-Wm;
251     E_b=Wo-Wb;
252     n_f=(Wo-Wf)/Wo;
253     n_m=(Wo-Wm)/Wo;
254     n_e=(Wo-We)/Wo;
255     n_b=(Wo-Wb)/Wo;
256 elseif Wf>Wo && Wf>Wm && Wf>Wb
257     E_e=Wf-We;
258     E_mov=Wf-Wm;
259     E_b=Wf-Wb;
260     n_f=(Wf-Wf)/Wf;
261     n_m=(Wf-Wm)/Wf;
262     n_e=(Wf-We)/Wf;
263     n_b=(Wf-Wb)/Wf;

```

```

264 else
265     E_e=Wm-We;
266     E_mov=Wm-Win;
267     E_b=Wm-Wb;
268     n_f=(Wm-Wf)/Wm;
269     n_m=(Wm-Win)/Wm;
270     n_e=(Wm-We)/Wm;
271     n_b=(Wm-Wb)/Wm;
272 end
273
274 end
275
276 %Written function for optimal control using LQR
277 function [kp,kd]=optcontrol()
278 m=5; %total mass of the damping device assembly
279 A=[0 1;0 0];
280 B=[0; -1/m];
281 Q=[0.1 0; 0 0.01];
282 R=1E8;
283 [G]=lqr(A,B,Q,R);
284 kp=G(1);
285 kd=G(2);
286 end
287
288 function [x0,tSpan]=iconds(Run_mode,PM,n,mode,loc)
289     w=PM(:,1);
290     %Initial conditions
291     if Run_mode~=5
292         x0=zeros(2*n+4+2,1); x0(end/2-2)=loc;
293     else
294         x0=zeros(2*n+8,1); x0(end/2-3)=loc; x0(end/2-1)=1-loc;

```

```

295         end
296         t0=0;%initial time
297         tf=30;%final time
298         dt=1/(2*w(mode));%timestep
299         tSpan=t0:dt:tf;
300
301     end
302     function [ParamBeam,ParamE,ParamRobot,ParamF,ParamMode,loc]=nondim(Run_mode,n,
        Te,L,m,EI,mode)
303
304     [Kp,Kd]=optcontrol(); %call optcontrol for optimal gains
305     %Parameters of the mobile damping robot
306     mc=0.2;%in-span mass
307     ma=4.8;%suspended mass
308     b=0;%inertor (not considered here)
309     kp=Kp;%proportional gain
310     kd=Kd;%derivative gain
311
312     %Parameters of the electromagnetic circuit
313     R=22.42;% resistance
314     Li=1.496;% inductance
315     C=0.003;% capacitance
316     q0=20;%
317     v0=1;
318
319     %Beam normalized parameters
320     wp=sqrt(EI/m)/L^2;
321     s=sqrt(Te*L^2/EI);
322
323     w=zeros(n,1); % Natural frequency of each mode
324     axialFrequency=zeros(n,1); % Axial frequency of each mode

```

```

325 for iii=1:n
326     w(iii)=(pi)^2*sqrt(iii^4+iii^2*s^2/(pi^2)); %Natural frequency of the mode
327     axialFrequency(iii)=sqrt((-s^2/2+sqrt(s^4/4+w(iii)^2)));
328 end
329 k=(w(mode)*wp)^2*ma;% spring constant %can only be calculated once we know w
330 %key parameter for different dampers
331 if Run_mode==3
332     kf=8;% force constant
333     kv=kf;% voltage constant
334     Cd=0;%damping constant
335 elseif Run_mode==4
336     k=0;
337     kf=0;
338     kv=kf;% voltage constant
339     Cd=0;%damping constant
340 else
341     kf=0;
342     kv=kf;% voltage constant
343     Cd=2.2;%damping constant
344 end
345
346 %Mobile damping robot normalized parameters
347 k=k*L^3/EI;
348 cd=Cd*L*sqrt(1/(m*EI));
349 %tau=0/L^2*sqrt(EI/m);
350 mc_=mc/m/L;
351 kp_=kp*L^3/EI;
352 kd_=kd*L/sqrt(m*EI);
353 ma_=ma/m/L;
354 b_=b/m/L;
355 va=0.1/v0;

```

```

356
357 %Electric circuit normalized parameters
358 kv_=kv*L/(Li*wp*q0);
359 kf_=kf*q0/sqrt(EI*m);
360 R_=R/(Li*wp);
361 C_=1/C/Li/wp^2;
362
363 d=0.028;
364 v=(w(mode)*wp)/2/pi*d/0.2;
365 rho=1.225;
366 cd_=3.2129;
367 f0=0.5*rho*d*cd_*v.^2;
368 amp_=f0*L^3/EI;%normalized amplitude
369 freq=w(mode)/2/pi*wp;
370
371 %keyboard
372 %loop length
373 vmax=7; %m/s
374 d=0.028;
375 fs=0.2*vmax/d;
376 lambda=sqrt((1/2)*(Te/(4*m*L/L*fs^2))+sqrt((Te/(4*m*L/L*fs^2))^2+pi^2*EI/fs^2))
    );
377 loc=85/100*lambda/L;
378
379 ParamBeam=[n;wp;s;L]; ParamE=[kv_;kf_;R_;C_]; ParamRobot=[k;cd;mc_;kp_;kd_;ma_
    ;va;b_];
380 ParamF=[freq;amp_]; ParamMode=[w,axialFrequency];
381 end
382
383 function [ParamBeam,ParamRobot,ParamF,ParamMode,loc]=nondim2(Run_mode,n,Te,L,m
    ,EI,mode)

```

```

384
385 [Kp,Kd]=optcontrol(); %call optcontrol for optimal gains
386 %Parameters of the mobile damping robot
387 mc=0.2;%in-span mass
388 ma=4.8;%suspended mass
389 b=0;%inertter (not considered here)
390 kp=1.0000e-04;%proportional gain
391 kd=0.010;%derivative gain
392 Cd=2.2;
393
394 v0=1;
395
396 %Beam normalized parameters
397 wp=sqrt(EI/m)/L^2;
398 s=sqrt(Te*L^2/EI);
399
400 w=zeros(n,1); % Natural frequency of each mode
401 axialFrequency=zeros(n,1); % Axial frequency of each mode
402 for iii=1:n
403     w(iii)=(pi)^2*sqrt(iii^4+iii^2*s^2/(pi^2)); %Natural frequency of the mode
404     axialFrequency(iii)=sqrt((-s^2/2+sqrt(s^4/4+w(iii)^2)));
405 end
406 k=(w(mode)*wp)^2*ma;% spring constant %can only be calculated once we know w
407
408 %Mobile damping robot normalized parameters
409 k=k*L^3/EI;
410 cd=Cd*L*sqrt(1/(m*EI));
411 mc_=mc/m/L;
412 kp_=kp*L^3/EI;
413 kd_=kd*L/sqrt(m*EI);
414 ma_=ma/m/L;

```

```

415 b_=b/m/L;
416 va=0.1/v0;
417
418 d=0.028;
419 v=(w(mode)*wp)/2/pi*d/0.2;
420 rho=1.225;
421 cd_=3.2129;
422 f0=0.5*rho*d*cd_*v.^2;
423 amp_=f0*L^3/EI;%normalized amplitude
424 freq=w(mode)/2/pi*wp;
425
426 %keyboard
427 %loop length
428 vmax=7; %m/s
429 d=0.028;
430 fs=0.2*vmax/d;
431 lambda=sqrt((1/2)*(Te/(4*m*L/L*fs^2)+sqrt((Te/(4*m*L/L*fs^2))^2+pi^2*EI/fs^2))
    );
432 loc=85/100*lambda/L;
433
434 ParamBeam=[n;wp;s;L]; ParamRobot=[k;cd;mc_;kp_;kd_;ma_;va;b_];
435 ParamF=[freq;amp_]; ParamMode=[w,axialFrequency];
436
437 end
438
439 function [xdt]=modelfun(t,x,ParamBeam,ParamRobot,ParamE,ParamF,ParamMode,count
    ,mode,loc)
440 %Note: q has the size of 2n+4, with first 2n for the modes and the last 4
441 %for the position and vib. displacement of the absorber. Force distribution
442 %is uniform. This ODE is modified for the directly planned motion towards the
    antinode.

```

```

443
444 n=ParamBeam(1);
445 wp=ParamBeam(2);
446 s=ParamBeam(3);
447 L=ParamBeam(4);
448
449 k=ParamRobot(1);
450 cd=ParamRobot(2);
451 %tau=0/L^2*sqrt(EI/m);
452 mc_=ParamRobot(3);
453 kp_=ParamRobot(4);
454 kd_=ParamRobot(5);
455 ma_=ParamRobot(6);
456 va=ParamRobot(7);
457 b_=ParamRobot(8);
458
459 kv_=ParamE(1);
460 kf_=ParamE(2);
461 R_=ParamE(3);
462 C_=ParamE(4);
463
464 freq=ParamF(1);
465 amp_=ParamF(2);
466
467 w=ParamMode(:,1);
468 axialFrequency=ParamMode(:,2);
469
470 FWind=sum(amp_.*sin(2*pi*freq*t/wp)); % Composed from various frequencies
471
472 xdt=zeros(2*n+4+2,1);
473 xdt(1:end/2,1)=x((end/2+1):end,1); % Displacement of the Cable Modes

```

```

474
475 q1=x(1:(end/2-3),1);
476 q1dt=x((end/2+1):(end-3),1);
477
478 q2=x((end/2-2):end/2-1,1);
479 q2dt=x((end-2):end-1,1);
480
481 q3=x((end/2),1);
482 q3dt=x(end,1);
483
484 phi=zeros(n,1); % Eigenfunction of each mode
485 phiInt=zeros(n,1); % Eigenfunction of each mode
486
487 for iii=1:n
488     phi(iii)=sqrt(2)*sin(axialFrequency(iii)*q2(1));
489     phiInt(iii)=-sqrt(2)/axialFrequency(iii)*(cos(axialFrequency(iii))-1); %
490     Eigenfunction over
491 end
492 %count=1;%
493 if count==1
494     pFinal=loc; %Final robot position reference
495 tFinal=pFinal/0.1;
496 if t<0
497     p=pFinal;
498     pdt=0;
499 elseif (t<(tFinal+0))
500     p=pFinal;%va*(t);
501     pdt=0;%va;
502 else
503     p=pFinal;

```

```
504     pdt=0;
505 end % Constant speed reference planning
506 elseif count==2 || count==3
507 pFinal=pi/2/axialFrequency(mode); %Final robot position reference
508 tFinal=pFinal/va;
509 td=loc/va;
510 if t<5
511     p=loc;
512     pdt=0;
513 elseif (t<(tFinal-td+5))
514     %p=pFinal;
515     p=loc+va*(t-5);
516     pdt=va;
517 else
518     p=pFinal;
519     pdt=0;
520 end % Constant speed reference planning
521 else
522     pFinal=loc; %Final robot position reference
523 tFinal=pFinal/0.1;
524 if t<0
525     p=pFinal;
526     pdt=0;
527 elseif (t<(tFinal+0))
528     p=pFinal;%va*(t);
529     pdt=0;%va;
530 else
531     p=pFinal;
532     pdt=0;
533 end % Constant speed reference planning
534 end
```

```

535
536 %keyboard
537 disSum=q1.'*phi;
538 velSum=q1dt.'*phi;
539
540 zeta=0.;
541
542 M1=eye(n)+1*mc_*(phi.*phi); % Beam inertia matrix
543 M2=diag([mc_,ma_+b_]); % Robot inertia matrix
544 q1ddt=M1\(-(w.^2).*q1-2*zeta*(w.*q1dt)...
545          -(k*(disSum-q2(2))+cd*(velSum-q2dt(2))+kf_*q3dt(1))*phi+FWind*phiInt
546          );
547 q2ddt=M2\[(kp_*(p-q2(1))+kd_*(-q2dt(1)));...
548          (k*(disSum-q2(2))+cd*(velSum-q2dt(2))+kf_*q3dt(1))];
549 q3ddt=(kv_*(velSum-q2dt(2))-R_*q3dt(1)-C_*q3(1));
550
551 xdt(end/2+1:end)=[q1ddt;q2ddt;q3ddt];
552
553
554 function [xdt]=modelfun2(t,x,ParamBeam,ParamRobot,ParamF,ParamMode,count,mode,
555          loc)
556
557 %Note: q has the size of 2n+4, with first 2n for the modes and the last 4
558 %for the position and vib. displacement of the absorber. Force distribution
559 %is uniform. This ODE is modified for the directly planned motion towards the
560 antinode.
561
562 n=ParamBeam(1);
563 wp=ParamBeam(2);
564 s=ParamBeam(3);
565 L=ParamBeam(4);

```

```

563
564 k2=ParamRobot(1);
565 c2=ParamRobot(2);
566 %tau=0/L^2*sqrt(EI/m);
567 m1=ParamRobot(3);
568 kp=ParamRobot(4);
569 kd=ParamRobot(5);
570 m2=ParamRobot(6);
571 va=ParamRobot(7);
572 b=ParamRobot(8);
573
574 k3=ParamRobot(1);
575 c3=ParamRobot(2);
576 %tau=0/L^2*sqrt(EI/m);
577 m3=ParamRobot(3);
578 kp=ParamRobot(4);
579 kd=ParamRobot(5);
580 m4=ParamRobot(6);
581 va=ParamRobot(7);
582 b=ParamRobot(8);
583
584 freq=ParamF(1); % Wind Force Frequency (Hz)
585 amp_=ParamF(2); % Wind Force Amplitude
586 %phase=ParamWind(:,3); % Wind Force Phase
587
588 w=ParamMode(:,1);
589 axialFrequency=ParamMode(:,2);
590
591 FWind=sum(amp_.*sin(2*pi*freq*t/wp)); % Composed from various frequencies
592
593 xdt=zeros(2*n+8,1);

```

```

594 xdt(1:end/2,1)=x((end/2+1):end,1); % Displacement of the Cable Modes
595
596 q1=x(1:(end/2-4),1);
597 q1dt=x((end/2+1):(end-4),1);
598
599 q2=x((end/2-3):end/2-2,1);
600 q2dt=x((end-3):end-2,1);
601
602 q3=x((end/2-1):end/2,1);
603 q3dt=x((end-1):end,1);
604
605 phi=zeros(n,1); % Eigenfunction of each mode
606 phi2=zeros(n,1); % Eigenfunction of each mode
607 phiInt=zeros(n,1); % Eigenfunction of each mode
608
609 for iii=1:n
610     phi(iii)=sqrt(2)*sin(axialFrequency(iii)*q2(1));
611     phi2(iii)=sqrt(2)*sin(axialFrequency(iii)*q3(1));
612     phiInt(iii)=-sqrt(2)/axialFrequency(iii)*(cos(axialFrequency(iii))-1); %
        Eigenfunction over
613 end
614
615 p1Final=pi/2/axialFrequency(mode); %Final robot position reference
616 tFinal=p1Final/va;
617 td=loc/va;
618 if t<5
619     p1=loc;
620 elseif (t<(tFinal-td+5))
621     %p=pFinal;
622     p1=loc+va*(t-5);
623 else

```

```

624     p1=p1Final;
625 end % Constant speed reference planning
626
627 p2Final=(1-loc)-pi/2/axialFrequency(mode); %Final robot position reference
628 tFinal=p2Final/va;
629 td=(1-loc)/va;
630 if t<5
631     p2=(1-loc);
632 elseif (t<(tFinal-td+5))
633     %p=pFinal;
634     p2=(1-loc)+va*(t-5);
635 else
636     p2=p2Final;
637 end % Constant speed reference planning
638
639 disSum=q1.'*phi;
640 velSum=q1dt.'*phi;
641
642 disSum2=q1.'*phi2;
643 velSum2=q1dt.'*phi2;
644
645 zeta=0;
646
647 M1=eye(n)+1*m1*(phi*phi.')+1*m1*(phi2*phi2. '); % Beam inertia matrix
648 M2=diag([m1;m2]); % First Robot inertia matrix
649 M3=diag([m3;m4]); % Second Robot inertia matrix
650 q1ddt=M1\(-(w.^2).*q1-2*zeta*(w.*q1dt)...
651     -(k2*(disSum-(q2(2)))+c2*(velSum-(q2dt(2))))*phi...
652     -(k3*(disSum2-(q3(2)))+c3*(velSum2-(q3dt(2))))*phi2...
653     +FWind*phiInt);
654 q2ddt=M2\[(kp*(p1-q2(1))+kd*(-q2dt(1)));...

```

```
655         (k2*(disSum-q2(2))+c2*(velSum-q2dt(2)))];
656 q3ddt=M3\[(kp*(p2-q3(1))+kd*(-q3dt(1)));...
657         (k3*(disSum2-q3(2))+c3*(velSum2-q3dt(2)))]];
658
659 xdt(end/2+1:end)=[q1ddt;q2ddt;q3ddt];
660 end
```